Icarus 405 (2023) 115680

Contents lists available at ScienceDirect

Icarus

journal homepage: www.elsevier.com/locate/icarus

The NC-CC dichotomy explained by significant addition of CAI-like dust to the Bulk Molecular Cloud (BMC) composition

Teng Ee Yap *, François L.H. Tissot

The Isotoparium, Division of Geological and Planetary Sciences, California Institute of Technology, Pasadena, CA 91125, USA

ARTICLE INFO

Keywords:
Early solar system
Mixing model
Ti, Cr, Fe, Ca isotopes
CC chondrites
CAIs

ABSTRACT

Nucleosynthetic isotope anomalies of planetary materials provide insight into their genetic ties, informing our understanding of early Solar System isotopic architecture and evolution. Isotope anomalies of non-carbonaceous (NC) and carbonaceous (CC) materials in multi-element space suggests their variability primarily emerged from mixing between several primordial nebular source regions in the nascent protoplanetary disk. In particular, it has been suggested that the elemental and isotopic compositions of CC meteorites reflect admixtures of NC-like, CI-like, and CAI-like components. Despite the plethora of elements for which isotope anomalies have been characterized, no mixing model has quantitatively reproduced CC meteorite compositions for more than two elements.

In this paper, we leverage the recent characterization of Fe isotope anomalies in NC and CC materials, as well as CAIs, to place new constraints on the evolution of the early Solar System and the origin of the CC chondrites. We first respond to the recent proposal, based on Fe isotope analyses of returned samples from Cb-type asteroid Ryugu, that Ryugu and CI chondrites are genetically distinct from NC and CC bodies, originating from a third "CI reservoir" beyond the location of the CC reservoir. Namely, we propose that the appearance of such a trichotomy in meteoritic heritages arises from the current lack of Fe isotope data for CC achondrites. We go on to present a self-consistent mixing model that explains the Ti, Cr, Fe, and Ca concentrations and isotope anomalies of the CM, CV, CO, CK, and CR chondrite groups *via* admixing of (i) elementally OC-like material, (ii) CI/Ryugu-like material, (iii) isotopically CAI-like dust, and (iv) CAIs *sensu stricto*. We find that the CAI-like dust constitutes a major and broadly constant fraction (~36%) of all CC chondrites, and identify the CI-like component with the bulk composition of the Solar System's parent molecular cloud, denoting it BMC for "Bulk Molecular Cloud." We interpret our results in the context of a qualitative model for early Solar System isotopic evolution.

1. Introduction

The isotopic compositions of meteorites shine light on the history of the Solar System (SS), yielding constraints on the origin and evolution of their parent bodies therein. Nucleosynthetic isotope anomalies, in particular, constitute robust tracers of genetic links between meteorite groups, resistant as they are to modifications by physicochemical processing (Dauphas and Schauble, 2016). Such anomalies have established that a fundamental dichotomy exists between non-carbonaceous (NC) and carbonaceous (CC) SS materials, thought to be broadly associated with inner and outer SS origins, respectively. This NC-CC dichotomy reflects the heterogeneous distribution of presolar carriers in the protoplanetary disk, and has been observed through the isotopes of elements with diverse geo- and cosmochemical behaviors. These include Cr, Ti (Warren, 2011), Fe (Schiller et al., 2020), Ca (Dauphas et al., 2014), Mo (Budde et al., 2016), and Zn (Steller et al., 2022; Savage et al., 2022), among many others (Burkhardt et al., 2021). Mass-independent variations in O are suggested to originate from isotope-selective photodissociation of CO in the solar nebula (Clayton, 2002), and display a continuum between NC and CC bodies. Nonetheless, when plotted against nucleosynthetic anomalies of other elements, they contribute to defined inter- and intra-reservoir trends and maintain the dichotomy, corroborating the finding that meteorites derive from two isotopically distinct reservoirs. Hf-W chronology of iron meteorites suggest that the NC and CC reservoirs were separated shortly (< 1 Myr) after the formation of Ca-Al-rich inclusions (CAIs) (Kleine et al., 2020).

Complementary to the study of meteorites, which arrive at Earth bereft of information regarding their provenance, sample return

* Corresponding author.
E-mail address: tyap@caltech.edu (T.E. Yap).

https://doi.org/10.1016/j.icarus.2023.115680
Received 27 March 2023; Received in revised form 11 June 2023; Accepted 14 June 2023
Available online 30 June 2023

missions such as Hayabusa2 (Watanabe et al., 2017) and OSIRIS-REx (Lauretta et al., 2017) offer the potential to anchor well-characterized meteorite groups to bodies visited by spacecraft, and thus aid in the contextualization of their isotopic, elemental, and mineralogical compositions. Recent analyses of samples returned by Hayabusa2 from Cb-type asteroid Ryugu showed that they bear the closest resemblance to CI chondrites in chemistry, mineralogy, and isotope anomalies (Yada et al., 2022; Yokoyama et al., 2022; Hopp et al., 2022a; Paquet et al., 2022), and that in Ti-Cr-O isotope space, Ryugu and CI chondrites define an endmember composition of the CC reservoir (Fig. 1). At the same time, Ryugu and CI chondrites exhibit identical Fe isotope anomalies, which appear distinct from those of other CC chondrites (Fig. 2). This observation has led to the proposal that Ryugu and CI chondrites differ from both NC and CC materials in genetic heritage, representing unique specimens derived from a third, rarely sampled "CI" reservoir located at greater heliocentric distances than the CC reservoir, in the vicinity of the birthplaces of Uranus and Neptune (Hopp et al., 2022a). In this scenario, limited material transport between the CI and CC reservoirs may be attributed to the formation of Saturn or Uranus, just as the rapid formation of Jupiter has been suggested to facilitate the separation between the NC and CC reservoirs (Kruijer et al., 2017). Alternatively, the division of disk materials into isotopically distinct reservoirs may simply reflect preferential planetesimal formation at distinct radii, as dictated by the position of principal sublimation lines (Lichtenberg et al., 2021; Morbidelli et al., 2022).

Regardless of the number of early SS reservoirs or the exact mechanism by which they were separated, their isotopic variability likely emerged from mixing between several primordial nebular source regions. The isotopically distinct compositions of these regions were controlled by presolar micron-sized dust, which were subsequently incorporated into early-formed planetesimals/meteorite parent bodies during the formation of the NC and CC reservoirs. Indeed, investigation of bulk meteorite isotope anomalies in multi-element space suggests that while intra- and inter-reservoir variability may reflect a plethora of superposed nebular processes, they are largely governed by admixing between such primordial components, during and/or immediately following the collapse of the molecular cloud core (Burkhardt et al., 2019, 2021; Nanne et al., 2019). In particular, previous studies have collectively suggested that the isotopic and elemental composition of CC meteorites reflect admixing of NC, CI-like, and isotopically CAI-like materials (including CAIs *sensu stricto*) (*e.g.*, Trinquier et al., 2009; Braukmüller et al., 2018; Alexander, 2019b; Burkhardt et al., 2019). Nonetheless, no model has synthesized the contributions from these studies to quantitatively reproduce CC chondrite compositions for more than two elements. Bryson and Brennecka (2021) demonstrated that Ti and Cr isotope anomalies and concentrations in CC chondrite groups may be reproduced from admixtures of ordinary/enstatite chondrite-like (OC/EC-like) material, CI material, and CAIs. As we will show, however, this three-component model cannot be extended to Fe (a major rock-forming element), inviting the development of a model that can self-consistently reproduce Ti, Cr, and Fe isotope anomalies and concentrations in CC chondrite groups.

In this paper, we leverage the recent characterization of Fe isotope anomalies in a range of NC and CC materials (Schiller et al., 2020; Hopp et al., 2022a, 2022b), as well as CAIs (Shollenberger et al., 2019) to place new constraints on the origin of CC chondrites and the evolution of the early SS. First, we closely examine the Ti-Cr-O-Fe isotope systematics of NC and CC meteorites, and propose that the apparent gap in Fe isotope anomalies between Ryugu/CI chondrites and other CC chondrites, and hence the appearance of a trichotomy in meteoritic heritages, simply arises from the current lack of Fe isotope data for CC achondrites. Given the CC intra-reservoir trend observed in Ti-Cr-O isotope space extends to Fe, the Fe isotope anomalies of the CC achondrites are expected to bridge the said gap, thereby removing the need to invoke an additional reservoir in discussing the large-scale isotopic architecture of the early SS. Second, we present a mixing model exploring how the Ti, Cr, and Fe composition of CC chondrite groups can be reproduced *via* admixing between four components from three isotopically distinct nebular source regions: (i) elementally OC-like material, (ii) CI chondrite-like (Ryugu-like) material, (iii) isotopically CAI-like "dust," and CAIs *sensu stricto*. We show that our model can be extended to Ca with modifications to the isotopic composition of the CAI-like dust and discuss our findings within the context of a qualitative physical model for how the NC and CC reservoirs came to be. Notably, we identify the CI-like component in our mixing model with the bulk composition of the SS parent molecular cloud, denoting it BMC for "Bulk Molecular Cloud."

2. Predicted Fe isotope anomalies of the CC achondrites

To date, >20 achondrites have been designated as carbonaceous by virtue of their Ti-Cr-O isotope systematics (Sanborn and Yin, 2019). It bears mention that several of these CC achondrites (*e.g.*, NWA 2994,

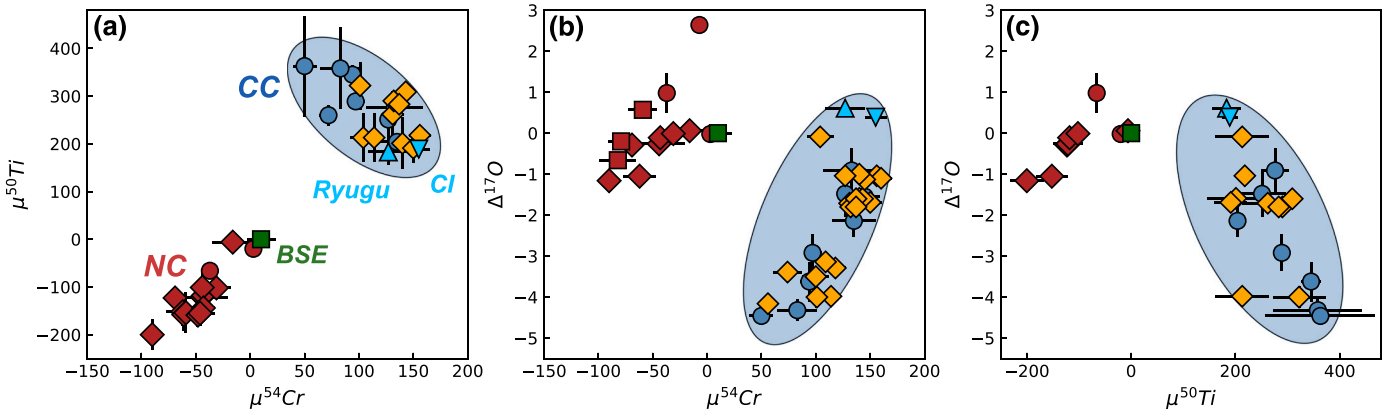

Fig. 1. Plots of (a) $\mu^{50}Ti$ *vs.* $\mu^{54}Cr$, (b) $\Delta^{17}O$ *vs.* $\mu^{54}Cr$, and (c) $\Delta^{17}O$ *vs.* $\mu^{50}Ti$ for NC (red) and CC (blue and orange) meteorites, the Bulk Silicate Earth (BSE), and Ryugu. Circles represent chondrites, diamonds achondrites, and squares NC iron meteorites (red) and the BSE (green). Plotted data show meteorite group means and standard errors (2SE) of the mean (95% CI). $\mu^{50}Ti$ and $\mu^{54}Cr$ values for CC chondrites, NC meteorites, and the BSE are taken from Yamashita et al. (2005, 2010), Shukolyukov and Lugmair (2006), Trinquier et al. (2007, 2009), Shukolyukov et al. (2009), Yamakawa et al. (2010), Qin et al. (2010), Göpel and Birck (2010), Petitat et al. (2011), Larsen et al. (2011), Zhang et al. (2011, 2012), Schiller et al. (2014), Sanborn and Yin (2015), Göpel et al. (2015), Van Kooten et al. (2016, 2020), Burkhardt et al. (2017), Goodrich et al. (2017), Gerber et al. (2017), Li et al. (2018), Mougel et al. (2018), Bischoff et al. (2019), Zhu et al. (2019, 2020, 2021), Williams et al. (2020), Schneider et al. (2020), Anand et al. (2021), Torrano et al. (2021), Metzler et al. (2021), and Dey et al. (2021). $\Delta^{17}O$ values for the CC chondrites, NC meteorites, and the BSE, are taken from the data compilation of Dauphas (2017) Data for Ryugu are taken from Yokoyama et al. (2022). Data for the CC achondrites (orange diamonds) are taken from sources provided in Supplementary Table 1.

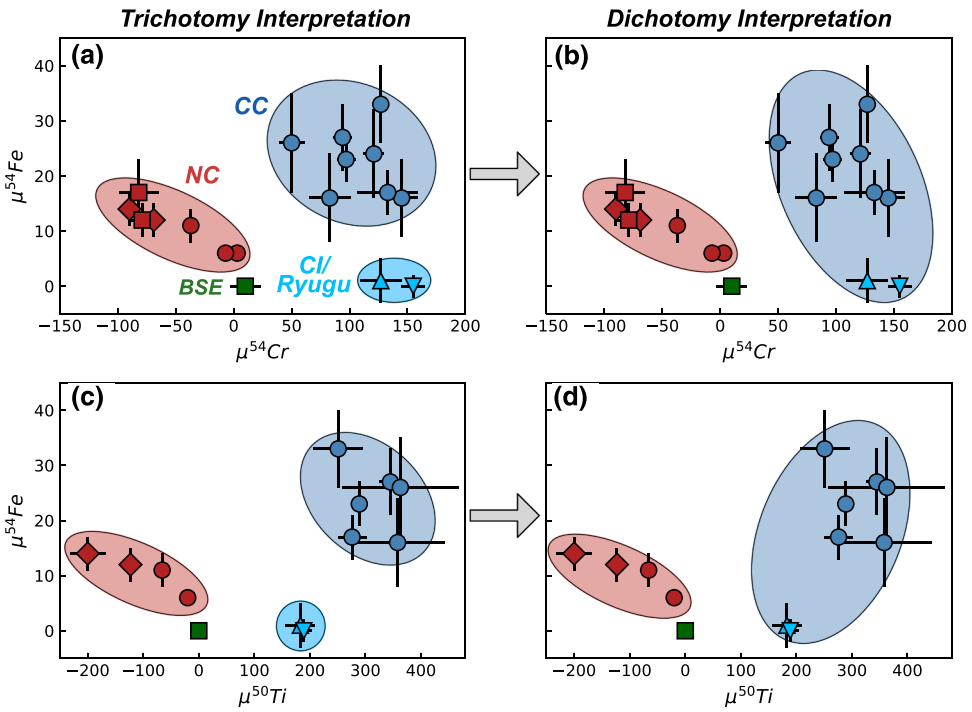

Fig. 2. Plots of (a and c) $\mu^{54}Fe$ *vs.* $\mu^{54}Cr$ and (b and d) $\mu^{54}Fe$ *vs.* $\mu^{50}Ti$ for NC and CC meteorites, the BSE, and Ryugu. The "Trichotomy" interpretation (a and b) is that adopted by Hopp et al. (2022a), whereby Ryugu and CI chondrites define a separate isotopic cluster from both NC meteorites and CC chondrites. In the "Dichotomy" interpretation (c and d), Ryugu and CI chondrites simply represent an end-member composition of the CC cluster in Fe isotope anomalies, as they do for O, Cr, and Ti isotope anomalies. Symbols as in Fig. 1. $\mu^{54}Fe$ values are taken from Schiller et al. (2020) and Hopp et al. (2022a, 2022b).

NWA 3100) have been found to possess rare and small relict chondrules, similar to some primitive achondrites (*i.e.,* acapulcoites and lodranites) (*e.g.,* Rubin, 2007; Neumann et al., 2018), and have been termed "highly-equilibrated chondrites" (Sanborn et al., 2019). In Ti-Cr-O isotope space, the CC achondrites are distributed along a common trend that spans from Ryugu/CI chondrites to the other CC chondrites (orange diamonds in Fig. 1; Table S1), with clear indication that all these meteorites define a single reservoir. This trend provides sufficient reason to expect the CC achondrites will exhibit Fe isotope anomalies between those of Ryugu/CI chondrites and the other CC chondrites. Our analysis here serves the purpose of stating this quantitatively, providing predicted/extrapolated $\mu^{54}Fe$ values for the CC achondrites.

While Hopp et al. (2022a) interpreted the apparent gap between Ryugu/CI chondrites and CC chondrites as evidence that the two represent distinct reservoirs (Fig. 2a, c), we assume *a priori* that they belong in the same CC reservoir (Fig. 2b, d). To predict the $\mu^{54}Fe$ of CC achondrites, we performed linear regressions through Ryugu, CI chondrites, and CC chondrites in both Fe-Cr and Fe-Ti isotope spaces, and then projected the measured $\mu^{54}Cr$ and $\mu^{50}Ti$ of the CC achondrites onto these regression lines (Fig. 3). The regression slopes obtained in Fe-Cr and Fe-Ti isotope spaces are ~−0.36 and +58.6, respectively. The predicted $\mu^{54}Fe$ from Fe-Cr isotope space range from +1.4 to +38.6, with a mean of +14.2 ± 4.3 (2SE), while those from Fe-Ti isotope space range from +1.0 to +27.8, with a mean of +13.1 ± 7.1 (2SE) (Table S3). Both these means fall between the mean $\mu^{54}Fe$ of Ryugu/CI chondrites (~0.5) and the CC chondrites (~22.8). The excellent agreement between the ranges of predicted $\mu^{54}Fe$ obtained in Fe-Cr and Fe-Ti isotope spaces (Fig. 3) supports a genetic relationship between Ryugu/CI chondrites and the other CC chondrites. A caveat to this proposition is that CC iron meteorites, which represent the earliest formed bodies like the CC

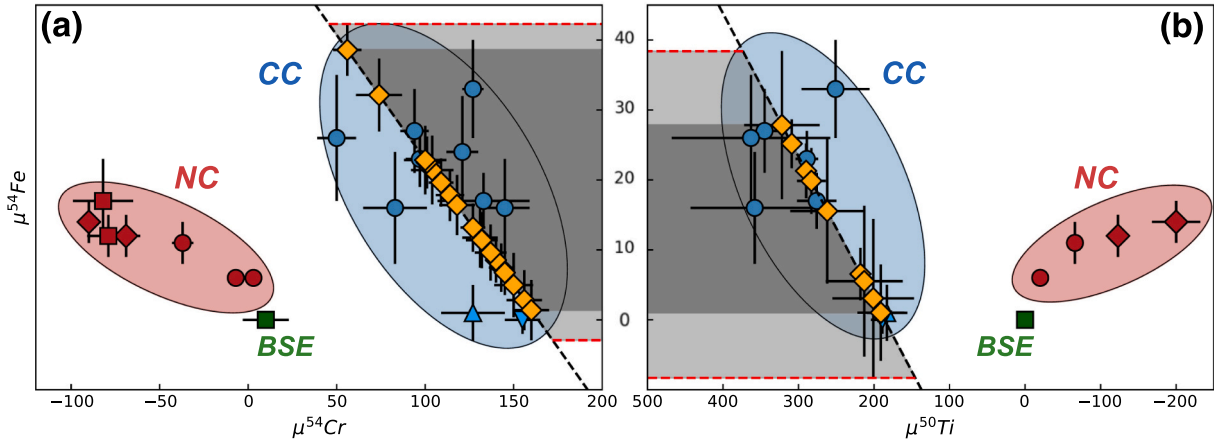

Fig. 3. Predicted $\mu^{54}Fe$ values for the CC achondrites in plots of (a) $\mu^{54}Fe$ *vs.* $\mu^{54}Cr$ and (b) $\mu^{54}Fe$ *vs.* $\mu^{50}Ti$.
Linear regressions through Ryugu, CI chondrites, and CC chondrites are performed accounting for errors in both $\mu^{54}Cr$ and $\mu^{50}Ti$ values (York-fit). Regions in dark (light) grey highlight the range of predicted mean $\mu^{54}Fe$ values (with errors considered). Red dotted lines indicate the projection of errors from the points with the highest and lowest $\mu^{54}Fe$ values onto the regression lines. Note the reversed x-axis scale in panel (b).

achondrites, exhibit Fe anomalies that cluster around those of CC chondrites and not the region between the CC chondrites and Ryugu/CI chondrites (Hopp et al., 2022b). We eagerly await future measurements of Fe anomalies in CC achondrites that will clarify this matter. As discussed below, while CI chondrites and Ryugu may not constitute a reservoir of their own, they may nonetheless represent a major population (and perhaps the earliest compositions) within the CC reservoir.

3. Mixing model for CC chondrites

CC chondrites have been suggested to originate from admixing of NC-, CI-, and CAI-like materials. Burkhardt et al. (2019), for instance, inferred that elemental and isotopic variations of refractory elements (*e.g.*, Ti, Sr, Ca) in bulk CC chondrites arise from mixing between OC/EC material and an isotopically CAI-like, but elementally chondritic component (denoted IC for Inclusion-like Chondritic). Similarly, the Ti and Cr isotope anomalies in CC chondrules can be explained by the addition of isotopically CAI- or Amoeboid Olivine Aggregate (AOA)-like material to NC-like chondrule precursors or dust (Gerber et al., 2017; Schneider et al., 2020). Braukmüller et al. (2018) analyzed moderately volatile and volatile elements in CC chondrites, and proposed that the matrices of CC chondrites derive from primitive CI-like material in addition to a more refractory "chondrule-related matrix." The inference that CC matrices consists of CI-like material is buttressed by more recent studies of Te, Rb, and K concentrations and isotope systematics between CC chondrite groups (Hellmann et al., 2020; Nie et al., 2021). Bryson and Brennecka (2021) quantitatively explored how the Ti and Cr isotope anomalies and concentrations in CC chondrite groups can be reproduced with a mixing model involving admixtures of OC/EC (NC) material, CI material, and CAIs. In their model, the Ti and Cr compositions of CC chondrite groups are treated as end products of two mixing steps—the first between NC and CI material, and the second between the products of NC-CI mixing (which we denote as "precursor" components) and CAIs (see also Trinquier et al., 2009).

Due to the low Fe concentration in CAIs, the three-component model of Bryson and Brennecka (2021) cannot be extended to Fe isotope anomalies and concentrations. This is evident in Fe-Ti isotope space, where the low Fe concentration would manifest as strongly curved mixing lines between the precursor components and CAIs, which would not pass through the CC chondrite groups (Fig. 4a) (Burkhardt et al., 2019). Even if the NC component is replaced with an NC-like component farther away from the CI chondrites, so as to expand the possible range of positions for the precursor components, the model would yield unrealistically large mass fractions of CAIs (Fig. 4b). Moreover, in $\mu^{54}Fe$ *vs.* Si/Fe (isotope-concentration) space, where the Fe/Si ratio is taken as a proxy for Fe enrichment, CAIs would plot far off to the right, away from both NC and CC meteorites (Fig. 4c). The inability of this three-component model (OC(EC)/CI/CAI) to explain the elemental and isotopic Fe systematics of CC chondrites indicate that an additional component, such as the IC component suggested by Burkhardt et al. (2019) or the similar Cryptic Refractory Dust (CRD) hypothesized by Charlier et al. (2019), needs to be considered beyond CAIs *sensu stricto*.

Most recently, Hellmann et al. (2023) demonstrated that the Te, Ti, and Cr isotopic compositions of CC chondrite groups may be explained by mixing between CI-like matrix material, chondrules, and refractory inclusions (*i.e.,* CAIs and AOAs). Instead of attributing variations in CC chondrite bulk compositions to mixing between their physical constituents, our model treats these variations as arising directly from mixing between nebular source regions hosting isotopically distinct presolar carriers in micron-sized dust. This amounts only to a philosophical difference. We make no assertion as to what physical form (chondrules, matrix, inclusions) the isotopically distinct components of our model take upon final incorporation into CC chondrite parent bodies, and are concerned only with reproducing the final bulk composition of the CC chondrites. The model proposed by Hellmann et al. (2023) can be thought of as capturing an intermediate stage in our model, with say, chondrules as a product of mixing between the nebular components here. Notably, while our model is centered on reproducing CC chondrite compositions, its broad framework also allows consideration of NC intra-reservoir variability, and the development of our qualitative model for early SS isotopic evolution later on.

3.1. Model description

The significance of Fe as a rock-forming element along with the recent characterization of Fe isotope anomalies in NC and CC meteorites (Schiller et al., 2020; Hopp et al., 2022a, 2022b) as well as in CAIs (Shollenberger et al., 2019) calls for a mixing model that can self-consistently reproduce the Ti, Cr, and Fe isotope anomalies and concentrations in CC chondrite groups. To this end, we developed a mixing model underpinned by the above studies to explore how admixtures of (i) elementally OC-like (for Ti, Cr, Fe, and later, Ca) material, (ii) CI material, (iii) isotopically CAI-like dust (an IC-like component), and (iv) actual CAIs can reproduce the Ti, Cr, and Fe composition of the CM, CV,

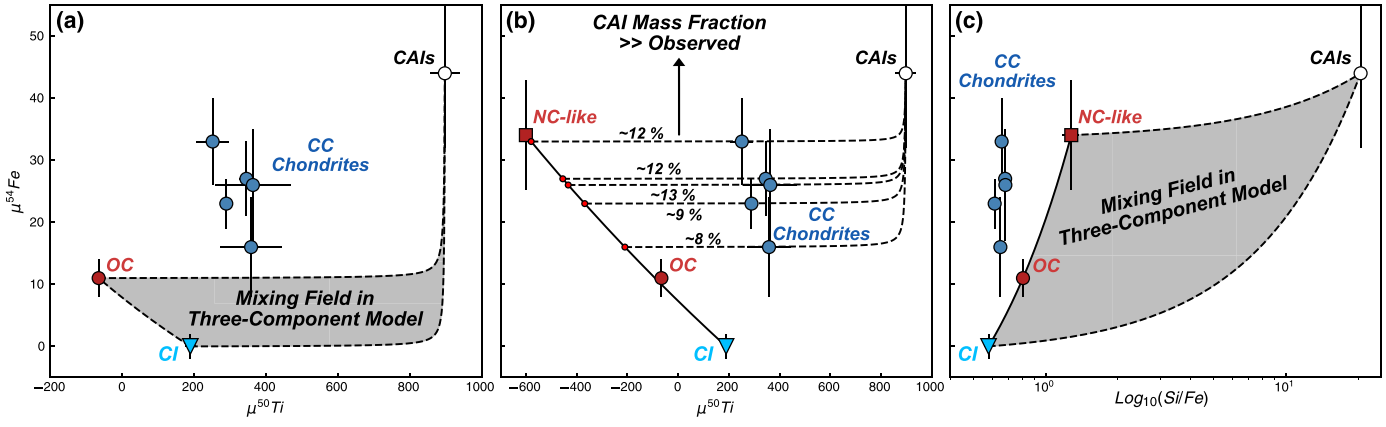

Fig. 4. Plots of $\mu^{54}Fe$ *vs.* $\mu^{50}Ti$ (a and b) and $\mu^{54}Fe$ *vs.* Si/Fe using the three-component (OC/EC, CI, CAI) mixing model adopted by Bryson and Brennecka (2021). In (a), the high Ti (and low Fe) abundance in CAIs induces strongly curved mixing lines that do not pass through the CC chondrite groups. In (b), if the OC chondrites are replaced by a NC-like component at high $\mu^{54}Fe$ (low $\mu^{50}Ti$), unrealistically large mass fractions of CAIs are required to explain the mixing of CC chondrites. Also, the position of the NC-like component constitutes a *upper (lower)* limit in $\mu^{50}Ti$ ($\mu^{54}Fe$). Note that the lowest $\mu^{50}Ti$ measured for a NC meteorite group is ~ −200. In (c), the CAIs plot far off to the right at high Si/Fe (~20.5), and precursor-CAI mixing lines do not pass through the CC chondrite groups. An alternative model is needed to explain the Fe systematics of the CC chondrites.

CO, CK, and CR chondrite groups. As mentioned above, these four components are presumed to represent isotopically distinct nebular dust, the mixing between which has established NC and CC intra- and inter-reservoir trends observed today.

In our mixing model, the final elemental and isotopic composition of each CC group is interpreted as the culmination of three mixing events, each between two components: (i) mixing between the OC-like and CI components into a so-called *precursor* component (Fig. 5a), (ii) mixing between the precursor component and CAI-like dust into a so-called *pre-CAI* component (Fig. 5b), and (iii) the addition of actual CAIs to the pre-CAI component (Fig. 5c). Together, there are four endmember components (*i.e.*, OC-like, CI, CAI-like dust, and CAIs) and two intermediate components (*i.e.*, precursor and pre-CAI). Note that the particular order in which these components are combined is irrelevant, having no effect on the final proportions of the four endmembers in each CC group.

Model input parameters, namely the isotope anomalies and concentrations of the OC chondrites, CI chondrites, CC chondrites, and CAIs, as well as the mass fractions of CAIs in each CC chondrite group, are provided in Table S2. CAI mass fractions are also reported in Table 1. Here, we outline the assumptions made in our mixing model (see Appendix for full details). Given the relationships between the six mixing components and available experimental constraints on their elemental and isotopic compositions, the only unknowns remaining are: (i) the isotope anomalies of the OC-like component; (ii) the elemental concentrations of the CAI-like dust components, and (iii) the mass fractions of CAI-like dust, CI material, and OC-like material incorporated into the five CC chondrite groups. Note that while the isotope anomalies of the CAI-like dust are assumed to be equivalent to those of CAIs in Ti-Cr-Fe isotope space, their elemental concentrations are allowed to vary between the five CC groups. This allows for the reproduction of CC chondrite compositions in a manner consistent with their observed abundances of CAIs, and enables insight into the composition of the yet unidentified dust. It is expected that the CAI source region harbored a range of elemental and isotopic compositions clustered about the specific values we adopt here, unlikely as it was to have been completely homogeneous.

To solve for the three unknowns, we make three assumptions. These assumptions are imposed in Fe-Ti isotope space, and the resulting constraints are carried forward into Ti-Cr and Fe-Cr isotope spaces and, eventually, into Ti-Ca, Fe-Ca, and Cr-Ca isotope spaces. To complement our mixing diagrams in isotope-isotope space, we also construct mixing diagrams in $\mu^{i}X$ *vs.* Si/X spaces, taking the ratio X/Si as a proxy for the enrichment of element X.

First, we assume that the OC-like component plots at a $\mu^{50}Ti$ value of −500 along a straight line passing through the OC and CI chondrites (Fig. 5). This fiducial value uniquely specifies the Cr and Fe (and later Ca) isotope anomalies of the OC-like component and likely represents a lower limit. The main conclusions of our study are hardly influenced by the exact position of the OC-like component, as will be discussed later on. With this assumption, we identify the OC-like component as an endmember of NC intra-reservoir mixing. While CI chondrites sit at the opposite end of the NC cluster in Ti-Cr-Fe isotope space, they cannot constitute the other endmember of NC mixing, as they do not lie along the NC trend when other elements (*e.g.*, Zr) are considered (Burkhardt et al., 2021) (see section "Nebular components in the forming Solar System" in Discussion). As such, the CI mixing component in our model is perhaps more appropriately termed "CI chondrite-like." For now, we omit this particularity, moving forward with "CI component" for the sake of clarity. Second, we assume that the Fe/Ti ratios of the CAI-like dust components are chondritic and equal to those of their respective precursor components. Graphically, this means that in Fe-Ti isotope space, the mixing lines between the precursor and CAI-like dust components are straight lines passing through the pre-CAI components (Figs. 5, 6). This assumption positions the precursor components along the CI-OC-like mixing line, allowing the determination of the mass fractions of CI and OC-like material incorporated into each CC chondrite group. Third, we assume that the Fe (and hence Ti) concentrations in the CAI-like dust components are equal to those of their respective precursor components. That is, the mass fraction of dust or precursor material in the pre-CAI components scales linearly with distance along the straight mixing lines. With this assumption, we are able to calculate the mass fraction of CAI-like dust incorporated into each CC chondrite group. The influence of these assumptions on the computed mass fractions of the four endmember components is assessed in the discussion (see section "Sensitivity to model assumptions").

3.2. Abridged procedure outline

Here, we provide a brief outline of how our mixing model is implemented (see Appendix for full details). In Fe-Ti isotope space, we first solve for the Fe and Ti concentrations and isotope anomalies of the pre-CAI components by "removing CAIs" from their respective CC chondrite

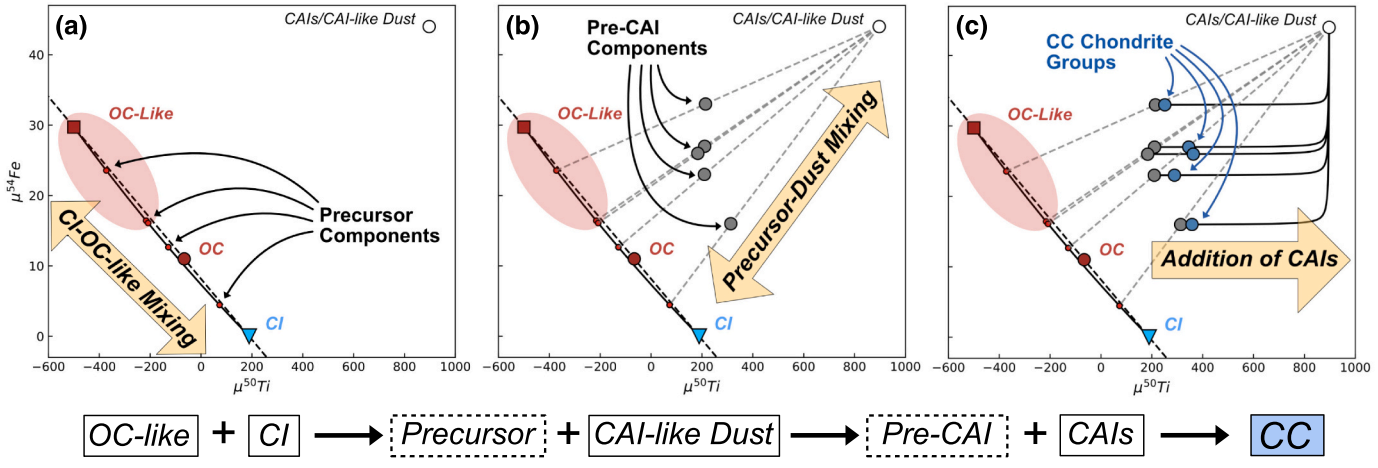

Fig. 5. Steps to creating the CC chondrites in our mixing model, involving (a) mixing between CI and OC-like material into so-called precursor components, (b) mixing between the precursor components and the CAI-like dust into so-called pre-CAI components, and (c) the addition of CAIs to the pre-CAI components. In the sequence below, the four endmember components and two intermediate components are boxed in solid and dashed lines, respectively. In our procedure (see Appendix for details), we start by taking an inverse approach to the sequence depicted here, solving first for the pre-CAI components, then for the precursor components, before using the latter to determine the mass fraction of dust incorporated into the former.

Table 1
Mixing model outputs.

CC Chondrite	Cumulative mass fractions *F* (%)			CAI-like dust weight ratios							ζ values (%)					
Groups	*CI*	*OC-like*	*Dust*	*Fe/Ti*	*Ti/Cr*	*Ti/Ca*	*Si/Ti*	*Si/Fe*	*Si/Cr*	*Si/Ca*	*Fe-Ti*	*Ti-Cr*	*Fe-Cr*	*Ti-Ca*	*Fe-Ca*	*Cr-Ca*
CM	**41.1**	**25.1**	**32.6**	**394.8**	**0.22**	**0.036**	**92.1**	**0.23**	**19.9**	**3.3**	**2.0**	**0.4**	**2.4**	**-23.4**	**-21.9**	**-23.7**
	+ 6.0	+ 4.5	+ 3.9	+ 7.3	+ 0.05	+ 0.006	+ 29.0	+ 0.08	+ 6.6	+ 1.1	-	-	-	-	-	-
	- 6.6	- 4.1	- 3.9	- 7.3	- 0.04	- 0.006	- 25.8	- 0.07	- 5.7	- 1.0	-	-	-	-	-	-
CV	**29.7**	**30.2**	**37.2**	**387.8**	**0.21**	**0.026**	**47.4**	**0.12**	**9.7**	**1.2**	**18.9**	**11.2**	**5.6**	**-40.7**	**-29.5**	**-33.2**
	+ 8.7	+ 5.5	+ 4.4	+ 8.4	+ 0.03	+ 0.007	+ 23.8	+ 0.06	+ 5.4	+ 0.8	-	-	-	-	-	-
	- 9.6	- 4.8	- 4.4	- 9.1	- 0.02	- 0.006	- 25.3	- 0.07	- 5.3	- 0.7	-	-	-	-	-	-
CO	**61.2**	**8.9**	**28.9**	**411.1**	**0.76***	**0.044**	**125.8**	**0.31**	**89.1***	**5.5**	**17.6**	**14.7**	**34.9**	**-11.4**	**4.2**	**-22.7**
	+ 10.0	+ 6.1	+ 6.3	+ 10.1	+ 1.50	+ 0.019	+ 39.2	+ 0.09	+ 201.1	+ 4.0	-	-	-	-	-	-
	- 10.3	- 5.6	- 6.3	- 9.4	- 0.36	- 0.013	- 40.2	- 0.10	- 51.1	- 2.5	-	-	-	-	-	-
CK	**31.4**	**30.5**	**34.0**	**388.4**	**0.25**	-	**36.8**	**0.09**	**9.2**	-	**16.9**	**-3.9**	**12.3**	-	-	-
	+ 12.3	+ 9.9	+ 7.3	+ 10.4	+ 0.15	-	+ 48.0	+ 0.12	+ 20.4	-	-	-	-	-	-	-
	- 13.6	- 8.5	- 7.4	- 11.4	- 0.08	-	- 63.6	- 0.16	- 14.6	-	-	-	-	-	-	-
CR	**12.9**	**40.6**	**45.9**	**375.2**	**0.16**	**0.054**	**136.9**	**0.36**	**22.3**	**7.4**	**-3.4**	**-0.1**	**-3.5**	**1.9**	**1.6**	**1.9**
	+ 11.4	+ 9.0	+ 5.6	+ 10.6	+ 0.03	+ 0.007	+ 27.6	+ 0.08	+ 5.6	+ 1.9	-	-	-	-	-	-
	- 13.3	- 7.3	- 5.6	- 12.7	- 0.02	- 0.006	- 26.1	- 0.07	- 5.1	- 1.7	-	-	-	-	-	-

* Median value from Monte Carlo simulation (~62% of trials) (see text in "Results").
Input mass fractions of actual CAIs are ~1.2% (CM), ~3.0 (CV), ~1.0 (CO), ~4.0 (CK), and ~0.6 (CR) (Rubin et al., 2011) Uncertainties reflect 1σ (84% CI).

groups. We then determine the positions of the precursor components along the CI-OC-like mixing line (Asm. I). These positions coincide with the intersections between the CI-OC-like mixing line and the straight precursor-dust mixing lines passing through the pre-CAI components (Asm. II). Next, we calculate the Fe and Ti concentrations of the precursor components as well as their mass fractions of incorporated CI/OC-like material. Finally, we calculate the mass fraction of CAI-like dust/precursor material incorporated into the pre-CAI components (with Asm. III). With the mass fractions of all six components in their respective mixing pairs determined, we determine the final mass fractions of the four endmember components (denoted *F* below) in each CC chondrite group (see Table 1).

Our treatment in Fe-Ti isotope space constrains all parameters but the Cr isotope anomalies and concentrations of the pre-CAI and precursor components, and the Cr concentrations of the CAI-like dust components. These can be determined in either Ti-Cr or Fe-Cr isotope space, where the Cr compositions of the pre-CAI components are also initially determined by "CAI removal." CI/OC-like and precursor/dust mass fractions determined from Fe-Ti isotope space are used to derive the Cr compositions of the precursor and CAI-like dust components. As a test of internal consistency in each two-isotope space (*i.e.*, Fe-Ti, Ti-Cr, Fe-Cr), we compare the elemental ratios of the pre-CAI components derived through the initial "removal of CAIs" to those retrieved using the mass fractions and elemental concentrations of CAI-like dust and precursor components. We denote the deviation of the latter from the former in % by ζ (Table 1). We defer the reader to the Appendix for an in-depth description of our procedure in isotope-isotope and isotope-concentration ($\mu^i X$ *vs.* Si/X) spaces, as well as the equations employed therein.

All model outputs along with their associated uncertainties are reported in Table S4. For each CC group, uncertainties were calculated *via* a Monte Carlo simulation ($n = 50{,}000$). Experimental constraints (*i.e.*, input parameters) are sampled at random from Gaussian distributions reflecting standard errors. All elemental concentrations of CAIs and CI, OC, and CC chondrites are assigned an error of 3% (2SE) for simplicity. We find it more meaningful to report uncertainties at the 1σ confidence level (16th and 84th percentiles) for two reasons: (i) the mixing model we propose, despite quantitative measures, is ultimately illustrative, and (ii) relatively large uncertainties in input parameters, coupled with the setup and assumptions of our model, yield wide and asymmetric distributions for several output parameters, most notably the mass fractions of CI material. A comparison between the distribution for the mass fraction of CI material and that of CAI-like dust obtained from the simulation is shown in Fig. 7. In Fig. 6a, the relatively low (and uncertain) $\mu^{54}Fe$ of the CO chondrites leads to ~38% of trials in which the $\mu^{54}Cr$ of the precursor component is between that of the pre-CAI and CAI-like dust components (Fig. 6b) (*i.e.*, no precursor-dust mixing line can cross the pre-CAI component in Ti-Cr and Fe-Cr isotope spaces). These trials are discarded in evaluating the uncertainties of parameters associated with the CO group.

4. Results

4.1. Ti-Cr-Fe isotope space

Our mixing model successfully explains the Ti, Cr, and Fe elemental and isotopic compositions of the five CC chondrite groups as end-products of mixing between elementally OC-like material, CI material, isotopically CAI-like dust, and CAIs *sensu stricto*. Key output parameters from our model, along with their associated uncertainties (1σ) are given in Table 1. The main results from our model are the cumulative mass fractions *F* (not *f*) of the four endmember components in each CC group. While the fraction of CI and OC-like material (F_{CI} and $F_{OC-like}$) vary widely across CC groups (ranging from $\sim 12.9^{+11.4}_{-13.3}$% (CR) to $\sim 61.2^{+10.0}_{-10.3}$% (CO) and from $\sim 8.9^{+6.1}_{-5.6}$% (CO) to $\sim 40.6^{+9.0}_{-7.3}$% (CR), respectively), the range of incorporated CAI-like dust (F_{Dust}) is relatively narrow, ranging from ~28.9 ± 6.3% (CO) to ~45.9 ± 5.6% (CR) with a mean of 35.7 ± 6.4(SD)%. Moreover, F_{Dust} is negatively correlated with F_{CAI} and F_{CI} (and thus positively correlated with $F_{OC-like}$).

The CAI-like dust components are assumed to have the same Ti and Fe concentrations as their respective precursor components (Asm. III), and have Fe/Ti ratios ranging from $\sim 375.2^{+10.6}_{-12.7}$ (CR) to $\sim 411.1^{+10.1}_{-9.4}$ (CO). Their Ti/Cr ratios, which are directly related to the mixing curvature required to link the dust, pre-CAI, and precursor components in Ti-Cr isotope space (Fig. 6b), range from $\sim 0.16^{+0.03}_{-0.02}$ (CR) to $\sim 2.06^{+1.03}_{-1.59}$ (CO). The abnormally large and uncertain Ti/Cr ratio of the CO group (Table 1, S4) is attributed to its proximity to the CI chondrites (yielding a strongly curved mixing line in Fig. 6b), and its large uncertainty in $\mu^{54}Fe$ (Fig. 6a).

All deviations between Fe/Ti and Ti/Cr ratios of the pre-CAI components derived through "CAI removal" and retrieved using f_{Dust} values (*i.e.*, $|\zeta_{Fe/Ti}|$ and $|\zeta_{Ti/Cr}|$) are <20%. $|\zeta_{Fe/Cr}|$ values for the CM, CV, CK, and CR groups are <20%, but that for the CO groups is ~35%. The OC-like component, given its fiducial $\mu^{50}Ti$ of −500, is positioned at a $\mu^{54}Fe$ of ~29.7 ± 4.4 and a $\mu^{54}Cr$ of $\sim -363.8^{+15.9}_{-16.6}$ when projected on the straight line passing through the OC and CI chondrites (Fig. 6).

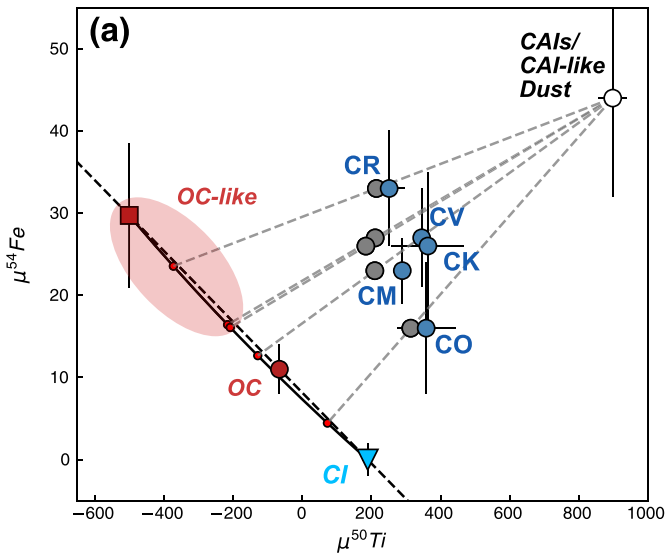

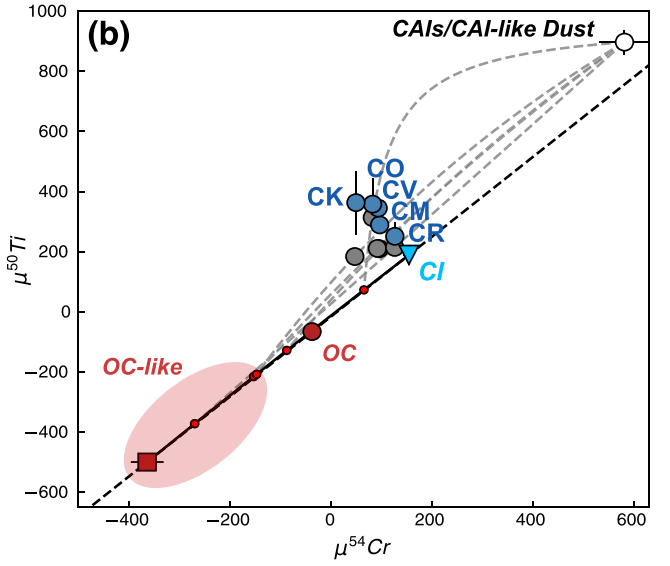

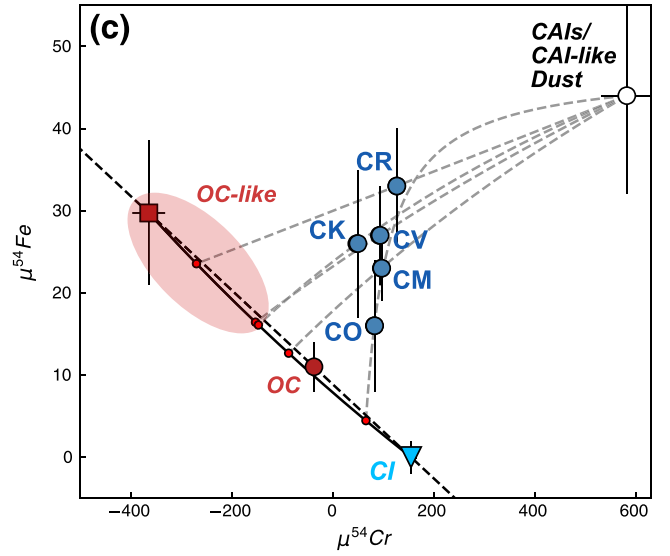

(caption on next column)

Fig. 6. Plots of (a) $\mu^{54}Fe$ *vs.* $\mu^{50}Ti$, (b) $\mu^{50}Ti$ *vs.* $\mu^{54}Cr$, and (c) $\mu^{54}Fe$ *vs.* $\mu^{54}Cr$ for the five CC chondrite groups (CM,CV,CO,CK,CR), CI chondrites, OC chondrites, the OC-like component, and CAIs/CAI-like dust. The red square designates the fiducial position of the elementally OC-like component, the actual position of which likely resides somewhere within the cropped ellipse. Precursor components are depicted as red points along the CI-OC-like mixing curve, and pre-CAI components as grey points adjacent to the CC chondrite groups (a and b). Grey and dashed mixing lines between the precursor components and the CAI-like dust components are shown. The latter shares the same isotopic signature as actual CAIs. Error bars reflect 2 standard errors of the mean (95% CI), and if not visible, are hidden behind symbols. Error bars are not shown for the precursor and pre-CAI components (see Table 1). The $\mu^{50}Ti$ value of CAIs is a mean of data taken from Williams et al. (2016), Davis et al. (2018), Burkhardt et al. (2019), Torrano et al. (2019), and Brennecka et al. (2020). The $\mu^{54}Cr$ value of CAIs is a mean of data taken from Papanastassiou (1986), Birck and Allègre (1988), Birck and Lugmair (1988), Bogdanovski et al. (2002), Trinquier et al. (2007), Mercer et al. (2010), Mane et al. (2016), and Torrano et al. (2018). Finally, the $\mu^{54}Fe$ value of CAIs is a mean of data taken from Shollenberger et al. (2019). (For interpretation of the references to colour in this figure legend, the reader is referred to the web version of this article.)

4.2. Isotope-concentration space

Our mixing model reproduces not only the Ti, Cr, and Fe isotope anomalies of the CC chondrite groups, but their Si/X ratios as well. In the absence of identified Si isotope anomalies, mixing diagrams of $\mu^{i}X$ *vs.* Si/X, where Si/X is taken as a proxy for enrichment in element X, provide means to account for constraints from the major rock-forming element (Fig. 8). The Si/Ti ratio of the OC-like component is $\sim 379.2^{+19.4}_{-18.9}$. The Si/Ti ratios of the CAI-like dust components range from $\sim 36.8^{+48.0}_{-63.6}$ (CK) to $\sim 136.9^{+27.6}_{-26.1}$ (CR), consistent with the dust being the less refractory counterpart of actual CAIs with Si/Ti ~ 15.9. Note that the relatively large uncertainty in the CK dust Si/Ti ratio is attributed to the large uncertainty in the $\mu^{50}Ti$ of CK chondrites.

The Si/Fe ratio of the OC-like endmember is ~1.19 ± 0.05. In Fig. 8b, the CAIs plot far off to the right at Si/Fe ~ 20.5, consistent with their low Fe concentrations. The CAI-like dust components have Fe/Ti ratios ranging from $\sim 375.2^{+10.6}_{-12.7}$ (CR) to $\sim 411.1^{+10.1}_{-9.4}$ (CO) (Table 1), which along with their Si/Ti ratios, yield Si/Fe ratios ranging from $\sim 0.09^{+0.12}_{-0.16}$ (CK) to $\sim 0.36^{+0.08}_{-0.07}$ (CR). All CC groups (and their pre-CAI components) fall within the region enclosed by the precursor-dust mixing lines and cross their respective lines within uncertainty (including uncertainties in the positions of precursor and CAI-like dust components).

The Si/Cr ratio of the OC-like endmember is $\sim 60.6^{+3.2}_{-3.1}$. In Fig. 8c, as in Fig. 8b, the CAIs plot far off to the right at Si/Cr ~ 250 owing to their low Cr concentrations. Compared to the other CC groups, the CO group is anomalous in both its high CAI-like dust Si/Cr ratio (≫100) and uncertainty (Table 1). The high Ti/Cr, and thus Si/Cr ratio of the CO group is a consequence of its low Cr concentration, which facilitates the significant curvature of its precursor-dust mixing line in Ti-Cr isotope space (Fig. 6b). The need for such curvature originates from the proximity of the CO group's precursor component to the CI chondrites, itself a consequence of our model assumptions. As mentioned above (see "Abridged procedure outline" in previous section), ~38% of trials in our Monte Carlo simulation for the CO group were discarded, as they yielded CO precursor component positions far too close to the CI chondrites to reproduce the pre-CAI component *via* addition of the CAI-like dust. The median of the distribution in CO dust Ti/Cr ratio from the remaining 62% of trials is $\sim 0.76^{+1.50}_{-0.36}$, almost a factor of three smaller than the value of ~2.06 obtained with the mean CO chondrite Ti and Fe isotopic compositions. The median in the distribution of CO dust Si/Cr ratio of trials is $\sim 89.1^{+201.1}_{-51.1}$, and we adopt this value in the mixing diagram of Fig. 8c. The large "positive" uncertainty (84th percentile of distribution)

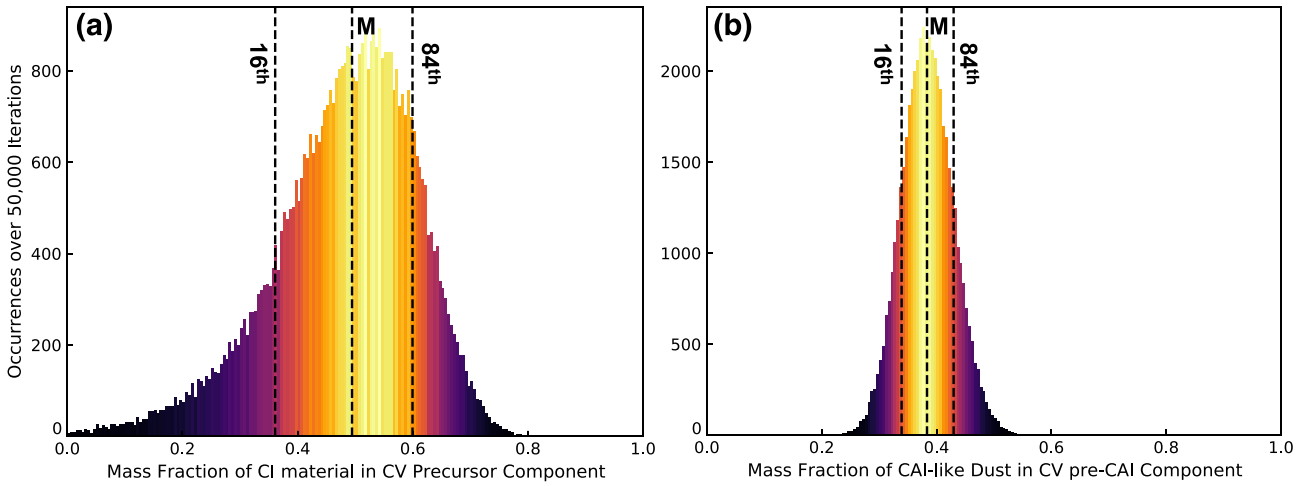

Fig. 7. Histograms of the mass fractions of (a) CI material and (b) CAI-like dust incorporated into the CV precursor component, created over 50,000 iterations in the Monte Carlo simulation. Black vertical dashed lines designate the median (M), the 16th percentile, and the 84th percentile (1σ) of the distributions. The mass fraction of dust is clearly better constrained than that of CI material.

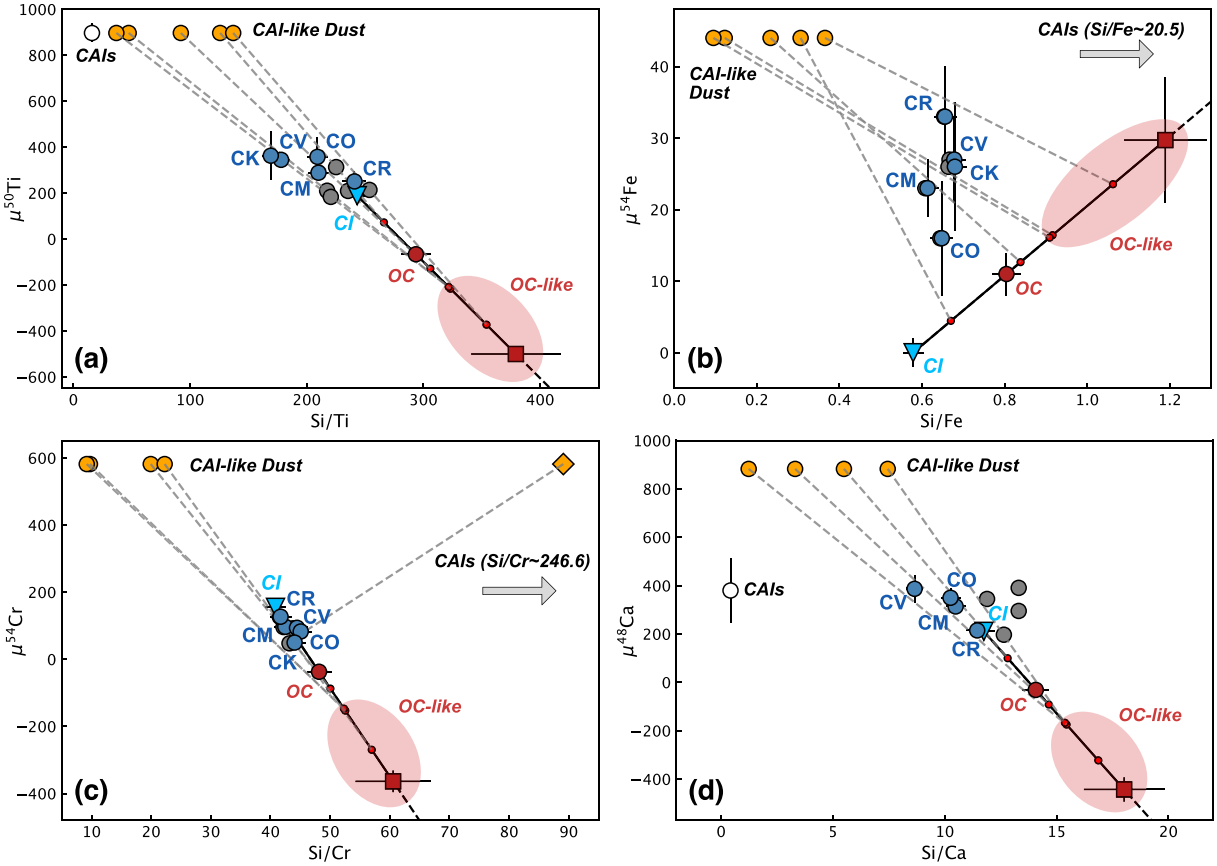

Fig. 8. Plots of (a) $\mu^{50}Ti$ *vs.* Si/Ti, (b) $\mu^{54}Fe$ *vs.* Si/Fe, (c) $\mu^{54}Cr$ *vs.* Si/Cr, and (d) $\mu^{48}Ca$ *vs.* Si/Ca for the five CC chondrite groups (CM,CV,CO,CK,CR), CI chondrites, OC chondrites, the OC-like component, and CAIs/CAI-like dust. Error bars shown for the OC (−like), CI, and CC chondrites reflect 2SE. Those for the CAI-like dust, precursor, and pre-CAI components are not shown for clarity (refer to Table 1). In (b) and (c), CAIs plot far off to the right at high Si/Fe and Si/Cr, owing to their depletion in Fe and Cr, respectively.

in this value highlight the increased sensitivity of Cr concentration to increased proximity of the precursor component to the CI chondrites. Omitting the CO chondrites, the CAI-like dust components have Ti-Cr ratios ranging from $\sim 0.16^{+0.03}_{-0.02}$ (CR) to $\sim 0.25^{+0.15}_{-0.08}$ (CK), which along with their Si/Ti ratios from above, yield Si/Cr ratios ranging from $\sim 9.2^{+20.4}_{-14.6}$ (CK) to $\sim 22.3^{+5.6}_{-5.1}$ (CR).

Our results indicate a correlation between $\mu^{i}X$ and enrichment in element X in the CC chondrites for Ti and Cr (and Ca). From Fig. 8, it is clear that the OC-like component is depleted in Ti, Fe, and Cr relative to other NC bodies. The CAI-like dust is enriched in Ti, Fe, and Cr relative

Table 2
Mixing endmember general features.

Endmember	General features	Similar component in literature
BMC (CI/BSE-like)	-Enriched in: (i) *s*-process nuclides and (ii) neutron-rich nuclides for elements up to and including Fe and Ni *(relative to NC)* -CI chondrite/solar-like elemental abundances	"Lost inner solar system material"[1]
CAIs	-Enriched in: (i) *r*-process nuclides and (ii) Ti and Ca *(relative to chondrites)* -Depleted in: Cr and Fe *(relative to chondrites)*	N/A
CAI-like Dust	-Enriched in: (i) *r* -process nuclides and (ii) Ti, Cr, Fe, and Ca *(relative to chondrites)*	Inclusion-like Chondritic (IC) component[2] Cryptic Refractory Dust (CRD)[3]
NC (OC-like)	-Depleted in: *s*-process nuclides -Enriched in: neutron-poor nuclides for elements up to and including Fe and Ni -OC/EC-like elemental abundances	Ureilite (-like)?

References: 1. Burkhardt et al. (2021); 2. Burkhardt et al. (2019); note that the IC component is elementally chondritic, unlike the CAI-like dust in this work, whose composition may be more refractory. 3. Charlier et al. (2019)

to NC and CC materials. For the highly refractory element Ti, the dust is intermediate between CAIs and the chondrites. For the moderately refractory elements Fe and Cr, however, the dust is more enriched than both chondrites and CAIs. While the dust is akin to the IC component (Burkhardt et al., 2019) in function, it is not elementally chondritic, and so more closely resembles the Cryptic Refractory Dust (CRD) from Charlier et al. (2019) (Table 2).

4.3. Extending our model to Ca

Nucleosynthetic Ca isotope anomalies result from variations in the neutron-rich nuclide ^{48}Ca, which like ^{50}Ti and ^{54}Cr, are thought to have been predominantly produced in rare Type-Ia supernovae (Clayton, 2003). Like Fe, the role of Ca as a major rock-forming element makes it an important target for the extension of any model attempting to explain the composition of bulk meteorites. As with Cr, the unknowns to be determined are the Ca concentrations and isotope anomalies of the precursor and pre-CAI components, as well as the Ca concentrations of the CAI-like dust components.

Our procedure in Ti-Ca isotope space (Fig. 9a) is largely the same as that in Ti-Cr isotope space (see Appendix), the sole difference being that the isotope anomalies of the dust and actual CAIs are not equivalent. In Ti-Cr-Fe isotope space, we assumed that the CAI-like dust and CAIs have identical anomalies. With Ca, this assumption needs to be relaxed as it results in precursor-dust mixing lines in $\mu^{48}Ca$ *vs.* Si/Ca space (Fig. 8d) that are not remotely close to the pre-CAI components.

This problem can be overcome by shifting the $\mu^{48}Ca$ of the CAI-like dust to values higher than the mean CAI $\mu^{48}Ca$ of ~380 ± 133, and more akin to those of some AOAs and CAIs that exhibit large ($\mu^{48}Ca >$ 700) Ca isotope anomalies (Bermingham et al., 2018; Valdes et al., 2021). AOAs, like most refractory inclusions, are likely genetically related to CAIs. In details, we projected the $\mu^{50}Ti$ of the CAI-like dust/CAIs onto the straight line passing through the OC and CI chondrites in Ti-Ca isotope space, and assumed the $\mu^{48}Ca$ value of that point for the dust (Fig. 9a). This value is $\sim 882.9^{+53.2}_{-50.9}$. With this modification to the Ca isotopic composition of the dust, the Ti/Ca ratios of the dust components range from $\sim 0.026^{+0.007}_{-0.006}$ (CV) to $\sim 0.054^{+0.007}_{-0.006}$ (CR), while their Si/Ca ratios range from $\sim 1.2^{+0.8}_{-0.7}$ (CV) to $\sim 7.4^{+1.9}_{-1.7}$ (CR). The precursor-dust mixing lines in $\mu^{48}Ca$ *vs.* Si/Ca space encompass the CC chondrite groups, but still fall short of their pre-CAI components (Fig. 8d). This

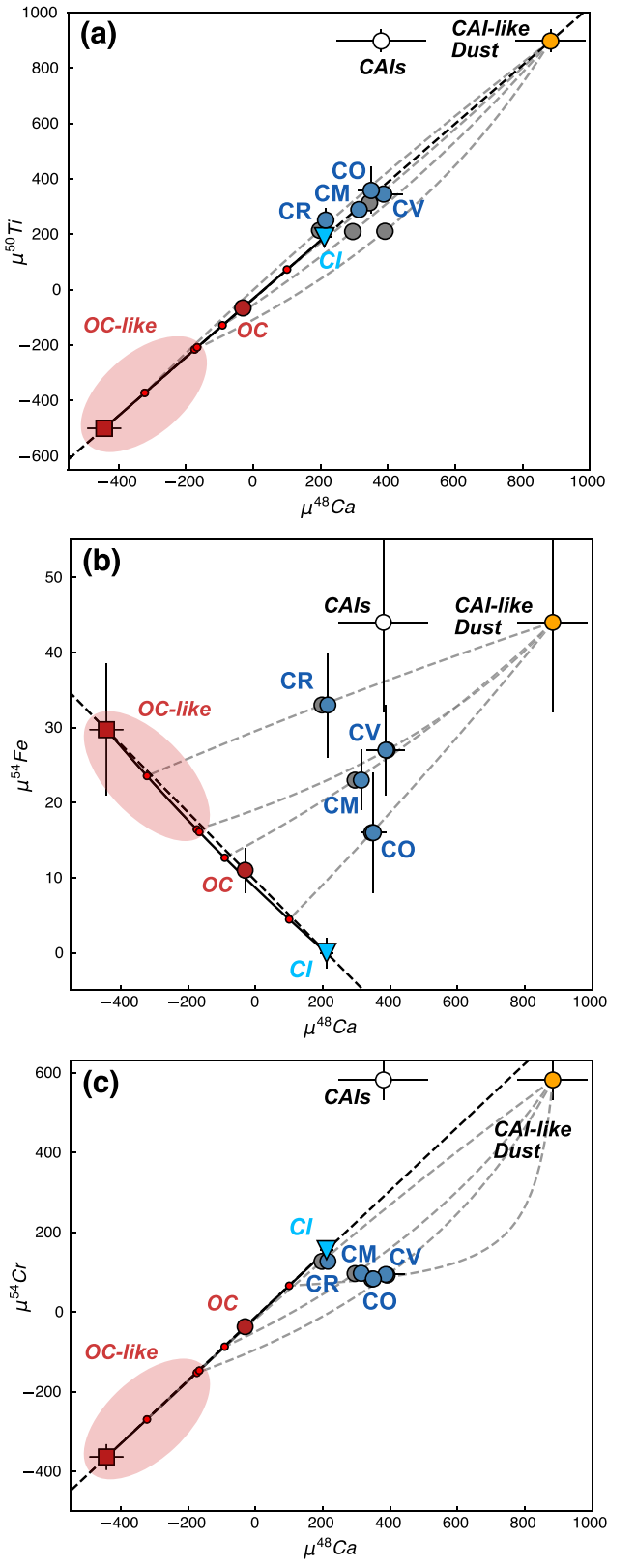

Fig. 9. Plots of (a) $\mu^{50}Ti$ *vs.* $\mu^{48}Ca$, $\mu^{54}Fe$ *vs.* $\mu^{48}Ca$. and (c) $\mu^{54}Cr$ *vs.* $\mu^{48}Ca$ for the five CC chondrite groups (CM,CV,CO,CK,CR), CI chondrites, OC chondrites, the OC-like component, and CAIs/CAI-like dust. Error bars reflect 2SE. $\mu^{48}Ca$ values for the CC chondrites, OC chondrites, and the BSE are taken from Dauphas et al. (2014), Huang and Jacobsen (2017), Schiller et al. (2015, 2018). The $\mu^{48}Ca$ value for CAIs is a mean of data taken from Chen et al. (2010), Huang et al. (2012), and Schiller et al. (2015).

discrepancy may be alleviated by shifting the OC-like component, positioned at a Si/Ca ratio of ~18.0 ± 0.9, slightly to higher Si/Ti (and thus Si/Ca) and/or higher $\mu^{48}Ca$ (which would shift the Si/Ca of the dust components to higher values). With the exception of the CV group, $|\zeta_{Ti-Ca}|$, $|\zeta_{Fe-Ca}|$, and $|\zeta_{Cr-Ca}|$ values are ≲30% (Table 1).

5. Discussion

5.1. Sensitivity to model assumptions

The key results from our mixing model are the mass fractions of each of the four endmember components incorporated into the CC chondrites. Here, we assess the sensitivity of the computed mass fractions to assumptions made in building the model. First is the isotopic composition of the OC-like component, which we positioned at a $\mu^{50}Ti$ value of −500 along a straight line passing through the CI and OC chondrites. Varying the position of the OC-like component along the straight CI-OC line (dashed in Fig. 6a) results in a change in the mass fractions of CI (and thus OC-like) material incorporated into the precursor components, and in turn, the mass fraction of incorporated dust. Nonetheless, changing its $\mu^{50}Ti$ by 100 only amounts to changes of <1% and <10% (absolute) in the final mass fractions of dust and CI material in the CC groups, respectively. Second is the assumption that the Fe/Ti ratios of the CAI-like dust components are equal to those of their respective precursor components, yielding straight mixing lines for the pre-CAI components. Upon changing the dust Fe/Ti ratios, the positions of the precursor components along the CI-OC-like mixing line must change as well, so as to ensure the precursor-dust mixing lines pass through their respective pre-CAI components. For each CC group, the new precursor position is that with a Fe/Ti ratio (from CI-OC-like mixing) that, along with the new Fe/Ti ratio of its dust component, constructs a mixing line that passes through their pre-CAI component. Increasing (decreasing) the dust Fe/Ti ratios—relative to the precursor Fe/Ti ratio—shifts the precursor components closer to the CI chondrites (OC-like component), which increases (decreases) the amount of CI material and CAI-like dust incorporated into the CC chondrites. Numerically, changing the Fe concentrations of the dust components by a factor of two results in changes of <8% and <15% (absolute) in the final mass fractions of dust and CI material incorporated, respectively. The last assumption was that the Fe and Ti concentrations of the CAI-like dust components (and thus their Fe/Ti ratios) are equal to those of their respective precursor components. We found that an increase in both concentrations by a factor of two (keeping their ratios constant) amounts to changes of <15% and <10% (absolute) in the final mass fractions of dust and CI material incorporated, respectively.

5.2. Nebular components of the forming solar system

The mixing model presented for the CC chondrite groups showcase how their Ti, Cr, Fe, and Ca concentrations and isotope anomalies may be explained *via* admixing between four primordial nebular components: an elementally OC-like (NC) component, CI chondrites (or a Ryugu-like component), isotopically CAI-like dust, and CAIs *sensu stricto*. This suggests the existence of at least three isotopically distinct source regions in the nascent/forming Solar System, corresponding to NC-like, CI-like, and CAI-like isotopic signatures. The variability in isotope anomalies within and between bodies from the NC and CC reservoirs is interpreted as the product of mixing between these source regions.

The CAI source consists of both CAIs *sensu stricto* as well as the suprachondritic CAI-like dust, which, relative to CAIs, is less enriched in the highly refractory Ti and Ca, but more enriched in the moderately refractory Cr and Fe (Fig. 8). Results from our mixing model indicate that ~30–45% of CAI-like dust was incorporated into CC chondrites, suggesting that such dust constitutes a major, if not the dominant, component of the CAI source. Our results also imply that this dust may not be isotopically equivalent to CAIs, and could exhibit isotope anomalies resembling those of some AOAs and hibonite-bearing refractory inclusions for elements such as Ca (Bermingham et al., 2018; Valdes et al., 2021).

It is conceivable that there are CAIs in CC matrices too small for identification by petrographic observations. In addition, CAIs and AOAs could have been reworked into chondrules, as suggested by recent oxygen isotope analyses of CV chondrules (Marrocchi et al., 2019). These complications imply that the CAI abundances we have used (to solve for the position of the pre-CAI components) are underestimates, translating to overestimates in CAI-like dust mass fractions. It should be noted, nonetheless, that the inclusion of unidentified and reworked CAIs will not obviate the need for the CAI-like dust in constructing a self-consistent model. If the true CAI abundances are ~10% (see Fig. 4b), removing the need for the dust in Fe-Ti isotope space (Fig. 6a), the model would not successfully be extended to Cr (Fig. 6b). It is also difficult to imagine that the mass fractions of CAI-like dust would change drastically upon account of these CAI sources, as they likely constitute a small fraction of the total CAI contribution. An interesting outcome of higher CAI abundances is higher Si/X ratios in Fig. 8, which would bring the elemental compositions of the CAI-like dust components closer to those of the CC chondrites.

Bulk anomalies within the NC reservoir display a clear and consistent trend in multi-element isotope space despite differences in nucleosynthetic origin and physicochemical behavior of their respective elements and perhaps presolar carriers (Burkhardt et al., 2021). This suggests that NC intra-reservoir variability is principally dominated by mixing between two isotopically distinct components (*e.g.,* Shuai et al., 2022). The OC-like component in our model is assumed to constitute an endmember composition of NC reservoir mixing. Above, it is positioned at a fiducial $\mu^{50}Ti$ of −500, more than twice the most negative Ti anomaly measured for an NC meteorite group (*i.e.*, Ureilites at ~−200; Trinquier et al., 2009; Williams et al., 2020). Such a low $\mu^{50}Ti$ for the OC-like component was chosen to accommodate the low $\mu^{50}Ti$ of the CR precursor component, and is unrealistic in consideration of the absence of samples with $\mu^{50}Ti$ between −500 and −200. Nonetheless, large uncertainties in the $\mu^{54}Fe$ of the CC chondrites and CAIs/CAI-like dust beget large uncertainties in the position of the precursor components. Graphically (Fig. 6a), it is plausible for the $\mu^{50}Ti$ of the CR precursor component to be as high as −200, permitting a higher $\mu^{50}Ti$ for the OC-like component as well. The exact position of the OC-like component has little influence on the mass fractions of CAI-like dust incorporated into the CC chondrites (see section "Sensitivity to model assumptions" above).

Finally, let us consider the CI endmember. In this work, focused on Ti-Cr-Fe-Ca isotopes, CI chondrites plot in the prolongation of the NC trend at the opposite end of the OC-like component (same end as the BSE) (Figs. 10a, c). As mentioned earlier, however, CI chondrites *sensu stricto* do not constitute the other endmember of NC intra-reservoir mixing, as they are offset from the NC trend when other elements such as Zr or Mo are considered (Fig. 10b) (Burkhardt et al., 2019, 2021). That is, there is a missing endmember and CI chondrites do not serve as a good approximation for it in multi-element isotope space. The BSE is peculiar in that it sits close to where this missing endmember is expected to be. Such an unsampled BSE-like endmember has been hinted at by Burkhardt et al. (2021), and several lines of evidence suggest that it cannot coincide with the CI chondrites *even in* Ti-Cr-Fe-Ca isotope space, as this would imply CI chondrites are devoid of CAI-like material. First, in isotope spaces where CI chondrites do not plot along the NC trend (*e.g.*, Zr-Ni, Mo-Ti), they plot among the other CC chondrites between the NC meteorites and CAIs/CAI-like dust (Fig. 10b). Second, petrographic analyses of the Ivuna CI1 chondrite have unambiguously identified a CAI (Frank et al, 2011) and an AOA (Kawasaki et al., 2022) in the meteorite. Anhydrous silicate grains in Ivuna and the Alais CI1 chondrite also exhibit O isotope compositions akin to AOAs, and two olivine grains in the former meteorite exhibit AOA-like MnO/FeO ratios (~1) (Morin et al., 2022). Third, material from comet Wild2 retrieved by the Stardust

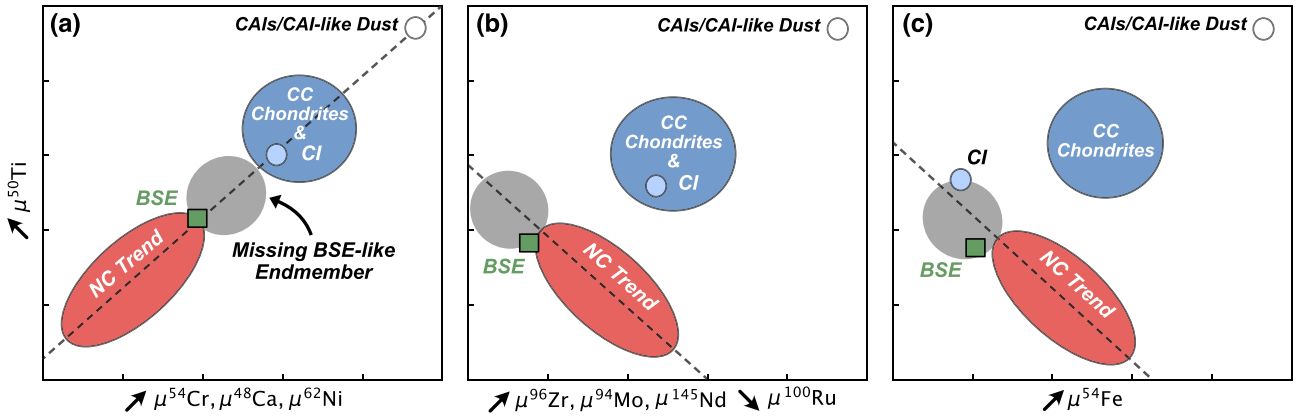

Fig. 10. Different configurations between the NC trend, CC reservoir, and CI chondrites in cross-sections of multi-element isotope space. (a) In Ti-(Cr, Ca, Ni) isotope space, the NC trend is aligned with the offset of CC materials towards CAIs, and points towards the CI chondrites. (b) In Ti-(Zr, Mo, Nd,-Ru) isotope space, the NC trend is not aligned with the CC offset and CI chondrites. (c) In Ti-Fe isotope space, the NC trend is not aligned with the CC offset, but points towards the CI chondrites. The missing BSE-like endmember is inferred to lie within the grey field at the end of the NC trend.

mission and inferred to be akin to Ryugu/CI-like material and interplanetary dust particles (*e.g.*, Zolensky et al., 2006; Berger et al., 2011; Kawasaki et al., 2022) have been found to possess CAIs (Joswiak et al., 2017). These observations indicate CI chondrites contain some degree of CAI-like material, perhaps predominantly present as CAI-like dust in their matrices (Bryson and Brennecka, 2021) and/or obscured by the extensive aqueous alteration to which their parent bodies were subjected. Moreover, these observations suggest the prominence of CAI-like material in the outer SS, and that the BSE-like endmember must be displaced from the CI chondrites away from CAIs/the CAI-like dust in Ti-Cr-Fe-Ca isotope space (Figs. 6, 9). This displacement would enable the precursor components of the CI chondrites to be positioned along the mixing line between the BSE-like and OC-like components. It would also provide additional leeway for the incorporation of CAI-like material into OC chondrites, several of which have been documented to possess CAIs (Bischoff and Keil, 1984; Kimura et al., 2022).

Additional information regarding the isotopic composition of the BSE-like endmember may be gleaned from the orientation of the NC trend with respect to the NC-CC offset towards CAIs in multi-element isotope space. From two-element isotope spaces, it is clear that the NC trend does not point in the direction of the CC meteorites and CAIs for all elements. In the case of heavy elements such as Zr, Mo, and Ru, intra-reservoir trends are governed by nucleosynthetic *s*-process variability and decoupled from the NC-CC offset (Fig. 10b), which for Mo is attributed to the excess of *r*-process material in CC meteorites (Dauphas et al., 2004; Fischer-Gödde et al., 2015; Akram et al., 2015; Budde et al., 2016; Poole et al., 2017). The isotope anomalies of lighter elements such as Ti, Cr, Ca, Ni, and Fe are attributed to quasi-equilibrium nucleosynthesis in supernovae (Clayton, 2003) and, aside from the latter, aligned with the NC-CC offset (Figs. 10a, c). The orientation of the NC trend is, of course, dependent on the details of normalization. That considered, it may be deduced that the unsampled BSE-like component is enriched in both *s-process* nuclides from asymptotic giant branch stars (resulting, for example, in low $\mu^{96}Zr$) and supernova-derived nuclides from quasie-quilibrium nucleosynthesis (*e.g.*, ^{50}Ti, ^{54}Cr) (Burkhardt et al., 2021), with the exception of ^{54}Fe. In other words, this component is enriched in neutron-rich nuclides of elements up to and including Fe and Ni, and neutron-poor nuclides of heavier elements. Based on the heliocentric gradient of isotope anomalies among NC meteorites, Burkhardt et al. (2021) postulated that this component derives from the innermost regions of the disk, where the probability of outwards scattering is low.

Of all meteorites, CI chondrites bear the closest resemblance to the solar photosphere in elemental composition (Barrat et al., 2012; Lodders, 2020). Keeping in mind that the Sun bears >99% of the SS mass, it is tempting to identify the BSE-like endmember (represented by CI chondrites in this work with Ti, Cr, Fe, and Ca) with the bulk SS, or solar composition. The complication here is that the Sun's oxygen isotopic composition inferred from solar wind captured by the Genesis spacecraft is drastically different from that of all planetary materials, including CI chondrites and Ryugu (McKeegan et al., 2011; Greenwood et al., 2023). In $\delta^{17}O$-$\delta^{18}O$ space, the Sun defines an endmember composition, separated from the Earth, Moon, Mars, and chondrites by hibonite-bearing refractory inclusions and CAIs. It is thus plausible that the solar isotopic composition is CAI-like, dominated by early infalling material (see "The origin of the NC & CC reservoirs" below). Here, we postulate that the BSE-like endmember represents the bulk composition of the SS *parent molecular cloud*, akin to the "unprocessed primitive cloud material" mentioned by Burkhardt et al. (2019). The designation of such a global component facilitates several key features of the qualitative model for early SS isotopic evolution we propose below. Namely, it allows us to simultaneously account for the heliocentric gradient observed within the NC reservoir in the inner SS (Burkhardt et al., 2019), and the composition of the CI chondrites in the outer SS. We henceforth denote the BSE-like endmember as BMC for "Bulk Molecular Cloud," and the OC-like component simply by NC. It is conceivable that the isotope anomalies of SS materials measured today reflect a combination of the "original" anomalies in presolar carriers upon ejection from previous generations of stars, and the BMC component. In Table 2, we provide a qualitative summary of the general features of the four endmember components in our mixing model, as well as components akin to them from previous literature. In Table 3, we provide our inferred isotopic and elemental compositions for the four endmember components.

5.3. The origin of the NC & CC reservoirs

The isotopic heterogeneity of the nascent SS may be attributed to either fractionation processes within the nebula, such as dust grain size-sorting and thermal processing (*e.g.,* Trinquier et al., 2009; Dauphas et al., 2010; Burkhardt et al., 2012), or changes in the composition of infalling material during the collapse of the molecular cloud core (*e.g.,* Nanne et al., 2019). These two scenarios are non-exclusive, but the dominance of the latter is supported by the observation that NC and CC inter- and intra-reservoir trends are not limited to a subset of isotope anomalies, but include elements across a wide range of geo−/ cosmochemical behavior. This is difficult to explain as the result of nebular processing of specific presolar carriers. Additional arguments in support of heterogeneous infall are provided by Burkhardt et al. (2019).

Here, we introduce a qualitative model for the origin of the NC and

Table 3
Mixing endmember inferred elemental and isotopic compositions.

Endmember	*Isotope anomalies*				*Elemental ratios*						
	μ^{50} *Ti*	μ^{54} *Cr*	μ^{54} *Fe*	μ^{48} *Ca*	*Fe/Ti*	*Ti/Cr*	*Ti/Ca*	*Si/Ti*	*Si/Fe*	*Si/Cr*	*Si/Ca*
BMC (CI/BSE-like)	189*	155*	0*	211*	420.5	0.17	0.048	243.2**	0.58*	40.8**	11.7**
	± 15	± 7	± 2	± 20	± 17.8	± 0.01	± 0.002	± 10.3	± 0.02	± 1.7	± 0.5
CAIs	897	582	44	380	0.78	15.5	0.026	15.9	20.5	246.6	0.42
	± 41	± 50	± 12	± 133	± 0.03	± 0.7	± 0.001	± 0.7	± 0.9	± 10.5	± 0.02
CAI-like Dust	*Similar to CAIs above*			~ 700-1000	*Specific to CC group (refer to Table 1)*						
NC (OC-like)	- 500**	**- 360****	**30***	**- 440****	364.7	0.16	0.048	**379.2***	**1.19***	**60.6***	**18.0***
	-	**± 33**	**± 9**	**± 50**	± 15.5	± 0.01	± 0.002	**± 38.3**	**± 0.10**	**± 6.3**	**± 1.8**

Bold values are model outputs, all other values are model inputs.
Uncertainties reflect 2σ (95% CI), and for elemental ratios, are computed assuming an error of 3% on elemental concentrations in our Monte Carlo simulation.
Actual values likely: *less than displayed, **greater than displayed. For the BMC endmember, differences are due to the presence of refractory material in CI chondrites. For the NC endmember, the current isotopic composition reflects a fiducial limit.

CC reservoirs from mixing between BMC, NC, and CAI source materials. This model builds on those of Burkhardt et al. (2019) and Nanne et al. (2019), in which the chronological order of infall at regions close to the young Sun translates to a spatial order in the newly formed disk, with the earliest infalling material being transported to the greatest heliocentric distance. Recent magnetohydronamic models of protostellar accretion indicate that changes in infalling material are natural in collapsing molecular clouds (Kuffmeier et al., 2023). At the onset of collapse, the molecular cloud contains two parcels of micron-sized dust corresponding to CAI-like and NC isotopic compositions, both amidst a "background" of BMC dust (Fig. 11a). The fact that CAIs are the oldest known solids in our SS suggests the former parcel constitutes early infalling material. The mineralogies and compositions of CAIs strongly suggest that they, and by extension the CAI source (with AOAs and other refractory inclusions), formed close to the young Sun before being transported outwards through viscous spreading of the forming disk and/or disk winds (Fig. 11b) (Wood, 2004; Ireland and Fegley Jr, 2000; Yang and Ciesla, 2012). Radial expansion of the disk leads to greater fractions of unprocessed cloud material, or BMC material, in its outer portions. This provides an explanation for the isotopic signatures of CI chondrites, which may primarily reflect the combination of CAI-like material and the BMC dust, with minimal contamination from NC material. If so, this beckons the question as to why CI chondrites appear so rare in our SS. Sears (1998) argued that CI chondrites may be the most abundant type of chondrites in our SS, severely underrepresented in meteoritic collections due to their low tensile strength, density, and thus likelihood of surviving passage through Earth's atmosphere. This claim is reinforced by studies that suggest the flux of meteorites constitutes only a meager (~1%) portion of material impacting the top of Earth's atmosphere (Bland et al., 1996; Drolshagen et al., 2017), the low tensile strength and density of Ryugu rocks (Grott et al., 2019), and the ubiquity of C-type asteroids in the main belt. Moreover, CC matrices are inferred to consists of CI-like material (see "Mixing Model for CC Chondrites" above). As Hopp et al. (2022a) suggested, CI chondrites may constitute the dominant bodies at the outskirts of the SS, where the probability of inward scattering is low. While CI chondrites and by extension Ryugu may not define a reservoir on their own, they are expected to be representative of the earliest bodies at the far reaches of the CC reservoir, in accord with their high volatile abundances.

The infall of the isotopically NC (OC-like in our mixing model) cloud parcel follows that of the CAI-like parcel (Fig. 11c), and is itself followed by BMC dust (Fig. 11d). The spatial order established from this one-dimensional infall model then, is "BMC, NC, CAI, BMC" outwards from the Sun. The adjacency of NC and CAI-like materials explains the covariance between the mass fractions of NC (OC-like) material $F_{OC-like}$ and CAI-like dust F_{Dust} in our mixing model. Mixing between the NC, and CAI-like, and BMC materials eventually gave rise to the isotopic signatures of the CC reservoir, while mixing between the BMC and NC materials at smaller heliocentric distances gave rise to the mixing trend observed in NC reservoir. Thus, the BMC facilitates both the formation of the CC reservoir in the outer SS, and the apparent heliocentric gradient within the NC reservoir (Burkhardt et al., 2021) in the inner SS. The lack of samples bridging the extensive gap between NC meteorites and the BMC (CI chondrites in Fig. 6; Fig. 9a, c) can be explained by the addition of $\lesssim$50% BMC material to predominantly NC material, or alternatively, the addition of $\gtrsim$50% NC material to predominantly BMC material.

Finally, the separation of the NC and CC reservoirs is facilitated by the early formation of Jupiter (Kruijer et al., 2017), and/or the preferential formation of planetesimals close to the silicate and water ice sublimation lines in the inner and outer SS (Morbidelli et al., 2022), respectively (Fig. 11e). In the latter scenario, and in the absence of Jupiter, the early forming planetesimals at the pressure bumps afforded by the sublimation lines sample NC and CC isotopic signatures before homogenization between the two reservoirs take place. Our model, which is the first to consider and explain the Fe and Ca systematics of CC chondrites, introduces a layer of complexity to that of Burkhardt et al. (2019) and Nanne et al. (2019) without forsaking any of its strengths, such as the ability to explain the abundance of refractory phases in the CC reservoir and the presence of non-CAI-like refractory precursors of Na-Al-rich chondrules in NC meteorites (Ebert et al., 2018). By invoking the BMC component, our model is able to account for the mixing trend in the NC reservoir and the anomalous Fe isotope anomalies of the CI chondrites, which cannot be explained by mixing between NC material and CAI-like dust alone.

6. Concluding remarks

Building on previous studies, we have developed a self-consistent mixing model in which the Ti, Cr, Fe, and Ca concentrations and isotope anomalies of CC chondrite groups are reproduced by admixing of elementally OC-like (for Ti, Cr, Fe, and Ca) material, CI material, isotopically CAI-like dust, and CAIs *sensu stricto*. Our model is novel in its quantitative extent, and represents an important step towards synthesizing the isotope anomalies of different elements into a coherent framework for physical interpretation. The key result from this model is the high mass fraction ($\gtrsim$30%) of CAI-like dust incorporated into the CC chondrites, suggesting CAIs and other isotopically anomalous refractory inclusions constitute only a small portion of the CAI source region in the early solar nebula. Having identified the BSE-like endmember of NC intra-reservoir mixing with the isotopic composition of the SS parent molecular cloud, we present a modified qualitative model for the isotopic evolution of the early SS and the origin of the NC and CC reservoirs therein. From this model, we expect material in the outer reaches of the SS (*i.e.*, around the Kuiper Belt) are isotopically CAI- and/or CI-like. Enticing avenues for future work include the extension of our mixing model to more elements for which nucleosynthetic anomalies have been characterized, and the development of a more sophisticated (*e.g.,* not "one-dimensional" as in Fig. 11) treatment of early SS isotopic evolution. This treatment should be underpinned by quantitative models of protoplanetary disk evolution, account for volatile element distributions in

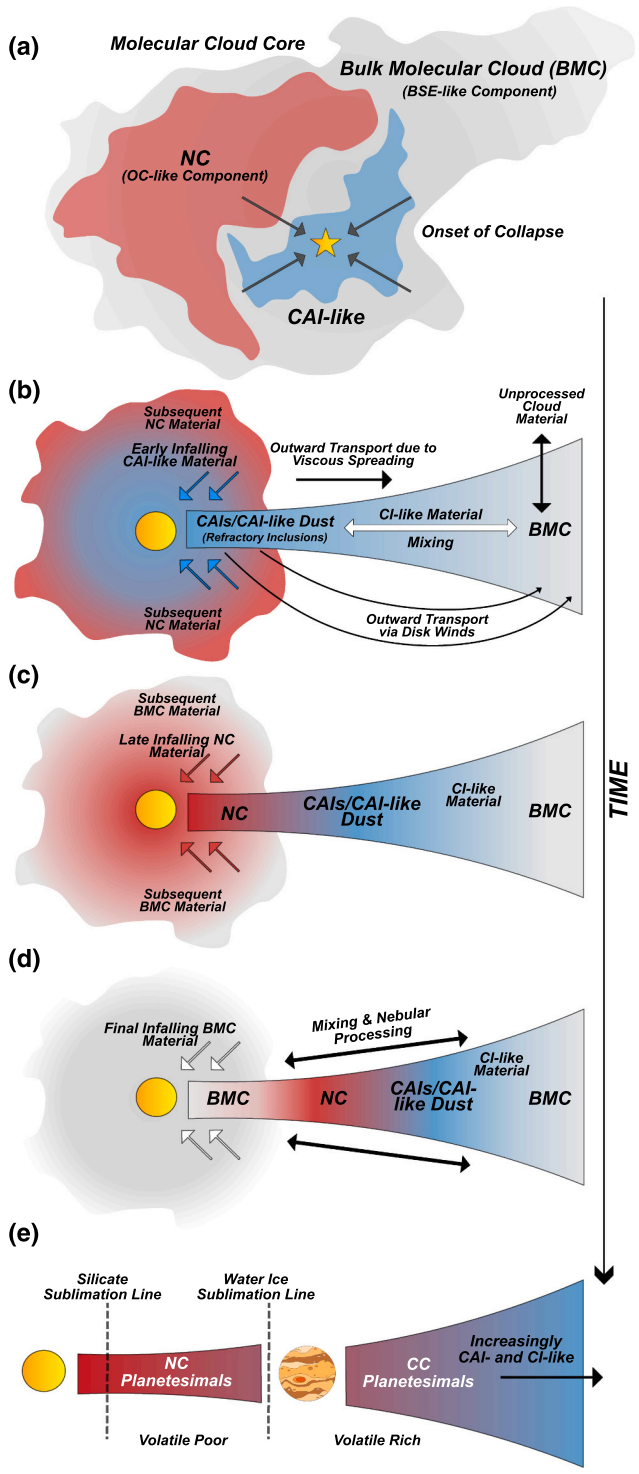

Fig. 11. Qualitative model for the origin of the NC and CC reservoirs. (a) At the onset of collapse, the molecular cloud contains two major parcels of micron-sized dust bearing NC (OC-like component) and CAI-like isotopic signatures. (b) Infall of the CAI-like parcel precedes that of the NC parcel due to the proximity of the former to the molecular cloud core. CAIs, the CAI-like dust, and other refractory inclusions are transported outwards from the young Sun due to viscous spreading of the disk and/or disk winds. Mixing between BMC material at the outer portions of the disk and the CAI-like materials yield CI chondrites. (c) NC material constitutes later infall, and precedes BMC material (d). (e) Mixing between BMC, NC, and CAI-like materials, in addition to nebular processing, establishes the NC and CC reservoirs. The reservoirs are kept separate by the early formation of Jupiter and/or early planetesimal formation at the silicate and water ice sublimation lines. See text for more in-depth discussion.

the early SS, and investigate the effects of disk/nebular processes beyond mixing that may have contributed to the elemental abundances and isotopic signatures observed in NC and CC SS materials.

Declaration of Competing Interest

The authors declare that they have no known competing financial interests or personal relationships that could have appeared to influence the work reported in this paper.

Data availability

Data used in study are provided in supplementary tables.

Acknowledgements

We thank Yves Marrocchi and one anonymous reviewer for constructive reviews that helped improve the manuscript, and editor Alessandro Morbidelli for prompt and careful editorial handling. We thank Christoph Burkhardt for providing the compilation of nucleosynthetic isotope anomalies from Burkhardt et al. (2021). This work was supported by a Packard Fellowship to FLHT.

Appendix A. Mixing model for CC chondrites

A.1. Model description

Here, we outline the details of our mixing model and how it is implemented in Ti-Cr-Fe isotope space. As mentioned above, there are four endmember components (*i.e.*, OC-like, CI, CAI-like Dust, and CAIs) and two intermediate components (*i.e.*, precursor and pre-CAI) in our model. The precursor and pre-CAI components are denoted by the subscripts P and PC in the variables below. Each CC chondrite group is interpreted as an end product of three mixing events: mixing between the OC-like and CI components to yield its precursor component (Fig. 5a), mixing between its precursor component and the CAI-like dust to yield its pre-CAI component (Fig. 5b), and the addition of CAIs to its pre-CAI component (Fig. 5c).

For each element X (*i.e.*, Ti, Cr, and Fe), each of the six components possesses an isotopic composition/anomaly (*i.e.*, the $\mu^{i}X$ value; denoted I^{X}) and a concentration (denoted C^{X}). Each CC group possesses its own isotopic composition/anomaly (I^{X}_{CC}) and elemental concentration (C^{X}_{CC}). The isotope anomalies and elemental concentrations of the OC-like component, CI component, and CAIs (*i.e.*, $I^{X}_{OC\text{-}like}$, I^{X}_{CI}, I^{X}_{CAI}, $C^{X}_{OC\text{-}like}$, C^{X}_{CI}, C^{X}_{CAI}) are invariant with respect to each CC group, while those of the intermediate components P and PC (*i.e.*, I^{X}_{P}, I^{X}_{PC}, C^{X}_{P} and C^{X}_{PC}) are group specific. The isotopic anomalies of the CAI-like dust components (*i.e.*, I^{X}_{Dust}) are not group specific, but their elemental concentrations (*i.e.*, C^{X}_{Dust}) are. For each CC group, each component contributes a mixing mass fraction (f) that, of course, is not element specific (*i.e.*, $f_{OC-like}$, f_{CI}, f_{Dust}, f_{CAI}, f_{P}, and f_{PC}).

Experimental constraints are given for I^{X}_{CC}, I^{X}_{CI}, I^{X}_{CAI}, $C^{X}_{OC\text{-}like}$, C^{X}_{CI}, C^{X}_{CAI}, and f_{CAI}, and are reported in Table S2. f_{CAI} values are also reported in Table 1. Cr, Ti, and Fe isotope anomalies of NC and CC chondrites are taken from sources listed in the captions of Figs. 1 and 2, while those of CAIs are listed in the caption of Fig. 6. It should be noted that there is considerable uncertainty regarding CAI Fe isotopic compositions (Shollenberger et al., 2019), given that most of the Fe in CAIs may be secondary. While we acknowledge this as a weak link in our mixing model, we stress the illustrative nature of our work and do not foresee its first-order results being altered dramatically by future, more reliable CAI Fe isotopic measurements to which we look forward. Concentrations of the three elements in the chondrites are taken from Alexander (2019a, 2019b). For CAIs, we used Cr, Ti, and Fe concentrations of

~381 ppm, ~5906 ppm, and ~4590 ppm, respectively. These concentrations reflect means from coarse-grained Type A CAIs measured by Grossman (1975), Grossman and Ganapathy (1976), Grossman et al. (1977) and Tissot et al. (2016), and are close to the Ti and Cr concentrations used by Trinquier et al. (2009) (*i.e.,* 5400 ppm and 200 ppm) as well as those in fine-grained CAIs, the most ubiquitous type of CAIs (MacPherson, 2014). Note that the Fe concentrations in fine-grained CAIs are typically in the wt%. We interpret these high concentrations as arising from significant alteration. Indeed, chondrite matrices are enriched in Fe, and given that (i) Fe is less refractory than Ti and Ca (Grossman and Larimer, 1974; Wood et al., 2019), and (ii) Ti concentrations in both coarse- and fine-grained CAIs typically fall below 1 wt%, there is good reason to be skeptical of fine-grained CAI Fe concentrations. This begs the question as to why the coarse- and fine-grained CAIs measured by Shollenberger et al. (2019) exhibit similar Fe isotope anomalies (Table S5). Should the latter not exhibit CI-like or CC-like Fe anomalies? A plausible hypothesis is that the secondary Fe in fine-grained CAIs is primarily inherited from the CAI-like dust, which bears the same Fe isotopic compositions as CAIs, but is much more enriched in Fe (Fig. 6a). The mean Si and Ca concentrations of Type A CAIs are ~93,936 ppm ~ 22,4275 ppm, respectively, and will be used in mixing diagrams complementary to those for Cr, Ti, and Fe below. The modal abundances (vol%) of CAIs in each CC group (CM ~ 1.2, CV ~ 3.0, CO ~ 1.0, CK ~ 4.0, CR ~ 0.6) are taken from Rubin (2011), and assumed to be mass fractions (wt%).

Omitting the elemental designation X, we have for mixing between CI and OC-like material:

$$f_{CI} = 1 - f_{OC-like}$$

$$C_P = C_{CI} f_{CI} + C_{OC-like} f_{OC-like} \tag{1}$$

$$I_P = \frac{I_{\mathrm{CI}} C_{\mathrm{CI}} f_{\mathrm{CI}} + I_{\mathrm{OC-like}} C_{\mathrm{OC-like}} f_{\mathrm{OC-like}}}{C_{\mathrm{CI}} f_{\mathrm{CI}} + C_{\mathrm{OC-like}} f_{\mathrm{OC-like}}} \tag{2}$$

For mixing between the precursor (P) component and CAI-like dust, we have:

$$I_{Dust} = I_{CAI}$$

$$f_{Dust} = 1 - f_P$$

$$C_{PC} = C_{Dust} f_{Dust} + C_P f_P \tag{3}$$

$$I_{PC} = \frac{I_{Dust} C_{Dust} f_{Dust} + I_P C_P f_P}{C_{Dust} f_{Dust} + C_P f_P} \tag{4}$$

Finally, for mixing between the pre-CAI (PC) component and CAIs, we have:

$$f_{CAI} = 1 - f_{PC}$$

$$C_{CC} = C_{CAI} f_{CAI} + C_{PC} f_{PC} \tag{5}$$

$$I_{CC} = \frac{I_{CAI} C_{CAI} f_{CAI} + I_{PC} C_{PC} f_{PC}}{C_{CAI} f_{CAI} + C_{PC} f_{PC}} \tag{6}$$

Given these relationships and available experimental constraints, there remain four unknowns: $I_{OC-like}$, C_{Dust}, f_{CI}, and f_{Dust}. In our treatment of the model, we make assumptions for the former three, and use the latter for tests of internal consistency. The assumptions are imposed in Fe-Ti isotope space and the resulting constraints, namely the Fe and Ti isotopic anomalies and concentrations of the two intermediate components and the mass fractions of all six components, are carried through the rest of the model.

A.2. Model assumptions

Assumption I. We impose the position of the elementally OC-like component along a straight line passing through the OC and CI chondrites in Ti-Cr-Fe isotope space, with the OC between it and the CI chondrites (Figs. 5, 6a). The isotopic composition of this endmember, $I^{X}_{OC-like}$, needs only be assumed for only a single element (*e.g.*, Ti), as the value for the other two elements (*i.e.*, Cr and Fe) are then uniquely specified along the OC-CI trend. We fix the μ^{50}Ti value of the OC-like component at a fiducial upper limit of −500, and acknowledge the wide range of its possible positions at the edge of the NC reservoir (Figs. 5, 6).

Assumption II. The Fe/Ti ratios of the CAI-like dust components are chondritic and equal to those of their respective precursor components, yielding straight precursor-dust mixing lines passing through the pre-CAI components in Fe-Ti isotope space (Figs. 5, 6a). This assumption positions the precursor components along the mixing curve between the OC-like and CI components, and thus constrains f_{CI} for each CC group given a fixed $I^{Ti,Fe}_{\mathrm{OC\text{-}like}}$. This in turn constrains f_{Dust} given $C^{Ti,Fe}_{Dust}$.

Assumption III. Finally, $C^{Ti,Fe}_{Dust}$ needs to be assumed for either Ti or Fe only, as ratios between Ti, Cr, and Fe concentrations in the CAI-like dust components can be derived from the available experimental constraints and our two prior assumptions. We assumed the Fe (and hence Ti) concentration in the CAI-like dust components are equal to those of their respective precursor components. This means the mass fraction of dust or precursor material in the pre-CAI components scales linearly with distance along the straight mixing lines.

A.3. Running the model

A.3.1. Mixing in Fe-Ti isotope space

Starting in Fe-Ti isotope space (Fig. 6a), the Fe and Ti concentrations and isotope anomalies of the pre-CAI components (*i.e.*, $C^{Ti,Fe}_{PC}$ and $I^{Ti,Fe}_{PC}$) are first solved for *via* Eqs. 5 & 6, respectively. Having thus "removed CAIs," straight mixing lines are constructed between the CAI-like dust and pre-CAI components (Asm. II), the intersections of which with the CI-OC-like mixing line determine the positions of the precursor components (*i.e.*, $I^{Ti,Fe}_{P}$).

The positions of the precursor components enable the calculation of the mass fraction of CI/OC-like material in them (*i.e.*, f_{CI}) *via* Eq. 2, and in turn their Fe and Ti concentrations (($i.e.$, $C_P^{Ti,Fe}$) *via* Eq. 1. Finally, the mass fraction of CAI-like dust contributed to the pre-CAI components (*i.e.*, f_{Dust}) is calculated assuming $C_{Dust}^{Ti,Fe} = C_P^{Ti,Fe}$ (Asm. III), and *via* Eq. 4.

Our treatment in Fe-Ti isotope space yields (i) the Fe and Ti concentrations and isotope anomalies of the precursor and pre-CAI components, and more importantly, (ii) the mass fractions of CI/OC-like and CAI-like dust/precursor material incorporated into the precursor and pre-CAI components, respectively. The six mass fractions from the three mixing pairs—OC-like and CI components, precursor components and CAI-like dust, pre-CAI components and actual CAIs—are used to compute the final mass fractions of the four endmember components in each CC group. We denote these final mass fractions by $F_{OC-like}$, F_{CI}, F_{Dust}, and $F_{CAI}(=f_{CAI})$ to distinguish them from mass fractions incorporated into the intermediate components. As a test of internal consistency, and by extension the validity of our assumptions, we compare the Fe/Ti ratios of the pre-CAI components derived through the initial "removal of CAIs" to those retrieved using f_{Dust}, $C_{Dust}^{Ti,Fe}$, and $C_P^{Ti,Fe}$ *via* Eq. 3. We quantify the deviation of the latter from the former in %, and denote this value ζ_{Fe-Ti}.

A.3.2. Mixing in Ti-Cr and Fe-Cr isotope spaces

The steps performed in the above provide all but the Cr isotope anomalies and concentrations of the precursor and pre-CAI components (*i.e.*, I_P^{Cr} I_{PC}^{Cr}, C_P^{Cr} C_{PC}^{Cr}), and the Cr concentration of the CAI-like dust components (*i.e.*, C_{Dust}^{Cr}). These remaining unknowns can be determined from either Ti-Cr or Fe-Cr isotope space.

In Ti-Cr isotope space (Fig. 6b), we solve for C_{PC}^{Cr} and I_{PC}^{Cr} by "removing CAIs" *via* Eqs. 5 & 6, respectively, as done for Ti and Fe. With f_{CI} for each CC group and the Cr isotope anomalies and concentrations of the CI and OC-like components, we calculate I_P^{Cr} *via*. Eq. 2. We proceed to solve for C_P^{Cr} *via* Eq. 1, and with f_{Dust} for each CC group, C_{Dust}^{Cr} *via* Eq. 4. As done in Fe-Ti isotope space, we quantify the deviation of the pre-CAI Ti/Cr ratios derived from the "removal of CAIs" to those retrieved using f_{Dust}, $C_{Dust}^{Cr,Ti}$, and $C_P^{Cr,Ti}$ *via* Eq. 3. This value is denoted ζ_{Ti-Cr}. Note that solving for $C_{Dust}^{Cr,Ti}$ *via* Eq. 3 and $C_{PC}^{Cr,Ti}$ would yield $\zeta_{Ti-Cr} = 0$, resulting instead in a mismatch between the CAI-like dust components between Fe-Ti, Ti-Cr, and Fe-Cr isotope spaces. We refrain from this approach to remain consistent in how we evaluate internal consistency.

The Cr, Ti, and Fe concentrations and isotope anomalies of the precursor, pre-CAI, and CAI-like dust components, as well as the mass fractions of all six components in their respective mixing pairs, are fully constrained through the procedure outlined above. For completeness, the mixing diagram for Fe-Cr isotope space (Fig. 6c) is constructed and ζ_{Fe-Cr} is calculated.

A.3.3. Mixing in $\mu^i X$ vs. Si/X space

To complement our work in isotope-isotope space above, we plot $\mu^i X$ against Si/X for Ti, Fe, and Cr, taking the ratio X/Si as a proxy for the enrichment of element X. Plotting Si/X instead of X/Si affords the benefit of straight mixing lines between all components. The mixing diagram for $\mu^{50}Ti$ *vs.* Si/Ti (Fig. 8A) is first used to constrain the Si/Ti ratios of the CAI-like dust components. The Fe/Ti ratios and Ti/Cr ratios for the dust components as derived from Fe-Ti and Ti-Cr isotope spaces above may then be used to calculate their Si/Fe and Si/Cr ratios, respectively, from which mixing diagrams for $\mu^{54}Fe$ *vs.* Si/Fe (Fig. 8B) and $\mu^{54}Cr$ *vs.* Si/Cr (Fig. 8C) can be constructed.

In $\mu^{50}Ti$ *vs.* Si/Ti, we project the $\mu^{50}Ti$ of the OC-like component onto the line connecting the CI and OC chondrites to determine its Si/Ti ratio. We proceed to project the $\mu^{50}Ti$ of the precursor components derived above onto the CI-OC-like mixing line to determine their Si/Ti ratios. To find the Si/Ti ratios of the pre-CAI components, we project the $\mu^{50}Ti$ of each pre-CAI component onto a line connecting the CAIs to their respective CC group. The Si/Ti ratios of each CAI-like dust component is then constrained by the intersection between the line passing through its respective precursor and pre-CAI components with the $\mu^{50}Ti$ of CAIs. In $\mu^{54}Fe$ *vs.* Si/Fe and $\mu^{54}Cr$ *vs.* Si/Cr, we follow the same steps as with Ti to determine the Si/Fe and Si/Cr ratios of the OC-like endmember, the precursor components, and pre-CAI components.

Appendix B. Supplementary data

Supplementary data to this article can be found online at https://doi.org/10.1016/j.icarus.2023.115680.

References

Akram, W., Schönbächler, M., Bisterzo, S., Gallino, R., 2015. Zirconium isotope evidence for the heterogeneous distribution of s-process materials in the solar system. Geochim. Cosmochim. Acta 165, 484–500.

Alexander, C.M.D., 2019a. Quantitative models for the elemental and isotopic fractionations in the chondrites: the non-carbonaceous chondrites. Geochim. Cosmochim. Acta 254, 246–276.

Alexander, C.M.D., 2019b. Quantitative models for the elemental and isotopic fractionations in chondrites: the carbonaceous chondrites. Geochim. Cosmochim. Acta 254, 277–309.

Anand, A., et al., 2021. Accretion and thermal evolution of IIAB and IIIAB iron meteorite parent bodies inferred from Mn-Cr chronometry. In: Lunar Planet. Sci. LII. Lunar Planet. Inst, Houston, p. 1498 (abstract).

Barrat, J.A., Zanda, B., Moynier, F., Bollinger, C., Liorzou, C., Bayon, G., 2012. Geochemistry of CI chondrites: major and trace elements, and Cu and Zn isotopes. Geochim. Cosmochim. Acta 83, 79–92.

Berger, E.L., Zega, T.J., Keller, L.P., Lauretta, D.S., 2011. Evidence for aqueous activity on comet 81P/Wild 2 from sulfide mineral assemblages in Stardust samples and CI chondrites. Geochim. Cosmochim. Acta 75 (12), 3501–3513.

Bermingham, K.R., Gussone, N., Mezger, K., Krause, J., 2018. Origins of mass-dependent and massindependent Ca isotope variations in meteoritic components and meteorites. Geochim. Cosmochim. Acta 226, 206–223.

Birck, J.L., Allègre, C.J., 1988. Manganese—chromium isotope systematics and the development of the early Solar System. Nature 331 (6157), 579–584.

Birck, J.L., Lugmair, G.W., 1988. Nickel and chromium isotopes in Allende inclusions. Earth Planet. Sci. Lett. 90 (2), 131–143.

Bischoff, A., Keil, K., 1984. Al-rich objects in ordinary chondrites: related origin of carbonaceous and ordinary chondrites and their constituents. Geochim. Cosmochim. Acta 48 (4), 693–709.

Bischoff, A., Barrat, J.A., Berndt, J., Borovicka, J., Burkhardt, C., Busemann, H., Zikmund, T., 2019. The Renchen L5-6 chondrite breccia–the first confirmed meteorite fall from Baden-Württemberg (Germany). Geochemistry 79 (4), 125525.

Bland, P.A., Berry, F.J., Smith, T.B., Skinner, S.J., Pillinger, C.T., 1996. The flux of meteorites to the Earth and weathering in hot desert ordinary chondrite finds. Geochim. Cosmochim. Acta 60 (11), 2053–2059.

Bogdanovski, et al., 2002. Cr isotopes in Allende Ca-Al-rich inclusions. In: Lunar Planet. Sci. XXXIII. Lunar Planet. Inst, Houston, p. 1802 (abstract).

Braukmüller, N., Wombacher, F., Hezel, D.C., Escoube, R., Münker, C., 2018. The chemical composition of carbonaceous chondrites: implications for volatile element depletion, complementarity and alteration. Geochim. Cosmochim. Acta 239, 17–48.

Brennecka, G.A., Burkhardt, C., Budde, G., Kruijer, T.S., Nimmo, F., Kleine, T., 2020. Astronomical context of Solar System formation from molybdenum isotopes in meteorite inclusions. Science 370 (6518), 837–840.

Bryson, J.F., Brennecka, G.A., 2021. Constraints on chondrule generation, disk dynamics, and asteroid accretion from the compositions of carbonaceous meteorites. Astrophys. J. 912 (2), 163.

Budde, G., Burkhardt, C., Brennecka, G.A., Fischer-Gödde, M., Kruijer, T.S., Kleine, T., 2016. Molybdenum isotopic evidence for the origin of chondrules and a distinct genetic heritage of carbonaceous and non-carbonaceous meteorites. Earth Planet. Sci. Lett. 454, 293–303.

Burkhardt, C., Dauphas, N., Tang, H., Fischer-Gödde, M., Qin, L., Chen, J.H., Papanastassiou, D.A., 2017. In search of the earth-forming reservoir: mineralogical, chemical, and isotopic characterizations of the ungrouped achondrite NWA 5363/NWA 5400 and selected chondrites. Meteorit. Planet. Sci. 52 (5), 807–826.

Burkhardt, C., Dauphas, N., Hans, U., Bourdon, B., Kleine, T., 2019. Elemental and isotopic variability in solar system materials by mixing and processing of primordial disk reservoirs. Geochim. Cosmochim. Acta 261, 145–170.
Burkhardt, C., Kleine, T., Dauphas, N., Wieler, R., 2012. Origin of isotopic heterogeneity in the solar nebula by thermal processing and mixing of nebular dust. Earth and Planetary Science Letters 357, 298–307.
Burkhardt, C., Spitzer, F., Morbidelli, A., Budde, G., Render, J.H., Kruijer, T.S., Kleine, T., 2021. Terrestrial planet formation from lost inner solar system material. Sci. Adv. 7 (52), eabj7601.
Charlier, B.L.A., Tissot, F.L.H., Dauphas, N., Wilson, C.J.N., 2019. Nucleosynthetic, radiogenic and stable strontium isotopic variations in fine-and coarse-grained refractory inclusions from Allende. Geochim. Cosmochim. Acta 265, 413–430.
Chen, H.W., et al., 2010. Calcium isotope anomalies in the Allende CAIs and the Angrite Angra Dos Reis. In: Lunar Planet. Sci. XLI. Lunar Planet. Inst, Houston, p. 2088 (abstract).
Clayton, R.N., 2002. Self-shielding in the solar nebula. Nature 415 (6874), 860–861.
Clayton, D., 2003. Handbook of Isotopes in the Cosmos: Hydrogen to Gallium, vol. 1. Cambridge University Press.
Dauphas, N., Schauble, E.A., 2016. Mass fractionation laws, mass-independent effects, and isotopic anomalies. Annu. Rev. Earth Planet. Sci. 44, 709–783.
Dauphas, N., Davis, A.M., Marty, B., Reisberg, L., 2004. The cosmic molybdenum–ruthenium isotope correlation. Earth Planet. Sci. Lett. 226 (3–4), 465–475.
Dauphas, N., Remusat, L., Chen, J.H., Roskosz, M., Papanastassiou, D.A., Stodolna, J., Eiler, J.M., 2010. Neutron-rich chromium isotope anomalies in supernova nanoparticles. Astrophys. J. 720 (2), 1577.
Dauphas, N., 2017. The isotopic nature of the Earth's accreting material through time. Nature 541 (7638), 521–524.
Dauphas, N., Chen, J.H., Zhang, J., Papanastassiou, D.A., Davis, A.M., Travaglio, C., 2014. Calcium-48 isotopic anomalies in bulk chondrites and achondrites: evidence for a uniform isotopic reservoir in the inner protoplanetary disk. Earth Planet. Sci. Lett. 407, 96–108.
Davis, A.M., Zhang, J., Greber, N.D., Hu, J., Tissot, F.L., Dauphas, N., 2018. Titanium isotopes and rare earth patterns in CAIs: evidence for thermal processing and gas-dust decoupling in the protoplanetary disk. Geochim. Cosmochim. Acta 221, 275–295.
Dey, et al., 2021. Exploring the planetary genealogy of Tarda - a unique new carbonaceous chondrite. In: Lunar Planet. Sci. LII. Lunar Planet. Inst, Houston, p. 2517 (abstract).
Drolshagen, G., Koschny, D., Drolshagen, S., Kretschmer, J., Poppe, B., 2017. Mass accumulation of earth from interplanetary dust, meteoroids, asteroids and comets. Planet. Space Sci. 143, 21–27.
Ebert, S., Render, J., Brennecka, G.A., Burkhardt, C., Bischoff, A., Gerber, S., Kleine, T., 2018. Ti isotopic evidence for a non-CAI refractory component in the inner Solar System. Earth Planet. Sci. Lett. 498, 257–265.
Fischer-Gödde, M., Burkhardt, C., Kruijer, T.S., Kleine, T., 2015. Ru isotope heterogeneity in the solar protoplanetary disk. Geochim. Cosmochim. Acta 168, 151–171.
Frank, et al., 2011. A CAI in the Ivuna CI1 chondrite. In: Lunar Planet. Sci. XLII. Lunar Planet. Inst, Houston, p. 2785 (abstract).
Gerber, S., Burkhardt, C., Budde, G., Metzler, K., Kleine, T., 2017. Mixing and transport of dust in the early solar nebula as inferred from titanium isotope variations among chondrules. Astrophys. J. Lett. 841 (1), L17.
Goodrich, C.A., Kita, N.T., Yin, Q.Z., Sanborn, M.E., Williams, C.D., Nakashima, D., Boyle, S., 2017. Petrogenesis and provenance of ungrouped achondrite Northwest Africa 7325 from petrology, trace elements, oxygen, chromium and titanium isotopes, and mid-IR spectroscopy. Geochim. Cosmochim. Acta 203, 381–403.
Göpel, C., Birck, J.L., 2010, June. Mn/Cr systematics: a tool to discriminate the origin of primitive meteorites. In: Goldschmidt Conference, 348.
Göpel, C., Birck, J.L., Galy, A., Barrat, J.A., Zanda, B., 2015. Mn–Cr systematics in primitive meteorites: insights from mineral separation and partial dissolution. Geochim. Cosmochim. Acta 156, 1–24.
Greenwood, R.C., Franchi, I.A., Findlay, R., Malley, J.A., Ito, M., Yamaguchi, A., Tsuda, Y., 2023. Oxygen isotope evidence from Ryugu samples for early water delivery to Earth by CI chondrites. Nat. Astron. 7 (1), 29–38.
Grossman, L., 1975. Petrography and mineral chemistry of Ca-rich inclusions in the Allende meteorite. Geochim. Cosmochim. Acta 39 (4), 433–454.
Grossman, L., Ganapathy, R., 1976. Trace elements in the Allende meteorite—I. Coarse-grained, Ca-rich inclusions. Geochim. Cosmochim. Acta 40 (3), 331–344.
Grossman, L., Larimer, J.W., 1974. Early chemical history of the solar system. Rev. Geophys. 12 (1), 71–101.
Grossman, L., Ganapathy, R., Davis, A.M., 1977. Trace elements in the Allende meteorite—III. Coarse grained inclusions revisited. Geochim. Cosmochim. Acta 41 (11), 1647–1664.
Grott, M., Knollenberg, J., Hamm, M., Ogawa, K., Jaumann, R., Otto, K.A., Moussi-Soffys, A., 2019. Low thermal conductivity boulder with high porosity identified on C-type asteroid (162173) Ryugu. Nat. Astron. 3 (11), 971–976.
Hellmann, J.L., Hopp, T., Burkhardt, C., Kleine, T., 2020. Origin of volatile element depletion among carbonaceous chondrites. Earth Planet. Sci. Lett. 549, 116508.
Hellmann, J.L., Schneider, J.M., Wölfer, E., Drazkowska, J., Jansen, C.A., Hopp, T., Kleine, T., 2023. Origin of isotopic diversity among carbonaceous chondrites. Astrophys. J. Lett. 946 (2), L34.
Hopp, T., Dauphas, N., Abe, Y., Aléon, J., O'D. Alexander, C.M., Amari, S., Yurimoto, H., 2022a. Ryugu's nucleosynthetic heritage from the outskirts of the Solar System. Sci. Adv. 8 (46), eadd8141.
Hopp, T., Dauphas, N., Spitzer, F., Burkhardt, C., Kleine, T., 2022b. Earth's accretion inferred from iron isotopic anomalies of supernova nuclear statistical equilibrium origin. Earth Planet. Sci. Lett. 577, 117245.
Huang, S., Jacobsen, S.B., 2017. Calcium isotopic compositions of chondrites. Geochim. Cosmochim. Acta 201, 364–376.
Huang, S., Farkaš, J., Yu, G., Petaev, M.I., Jacobsen, S.B., 2012. Calcium isotopic ratios and rare earth element abundances in refractory inclusions from the Allende CV3 chondrite. Geochim. Cosmochim. Acta 77, 252–265.
Ireland, T.R., Fegley Jr., B., 2000. The solar system's earliest chemistry: systematics of refractory inclusions. Int. Geol. Rev. 42 (10), 865–894.
Joswiak, D.J., Brownlee, D.E., Nguyen, A.N., Messenger, S., 2017. Refractory materials in comet samples. Meteorit. Planet. Sci. 52 (8), 1612–1648.
Kawasaki, N., Nagashima, K., Sakamoto, N., Matsumoto, T., Bajo, K.I., Wada, S., Yurimoto, H., 2022. Oxygen isotopes of anhydrous primary minerals show kinship between asteroid Ryugu and comet 81P/Wild2. Sci. Adv. 8 (50), eade2067.
Kimura, M., Greenwood, R.C., Komatsu, M., Imae, N., Yamaguchi, A., Sato, R., 2022. Petrology and classification of A-9003, A 09535, and Y-82094: a new type of carbonaceous chondrite. Meteorit. Planet. Sci. 57 (2), 302–316.
Kleine, T., Budde, G., Burkhardt, C., Kruijer, T.S., Worsham, E.A., Morbidelli, A., Nimmo, F., 2020. The non-carbonaceous–carbonaceous meteorite dichotomy. Space Sci. Rev. 216, 1–27.
Kruijer, T.S., Burkhardt, C., Budde, G., Kleine, T., 2017. Age of Jupiter inferred from the distinct genetics and formation times of meteorites. Proc. Natl. Acad. Sci. 114 (26), 6712–6716.
Kuffmeier, M., Jensen, S.S., Haugbølle, T., 2023. Rejuvenating infall: a crucial yet overlooked source of mass and angular momentum. Eur. Phys. J. Plus 138 (3), 1–13.
Larsen, K.K., Trinquier, A.N.N.E., Paton, C., Schiller, M., Wielandt, D., Ivanova, M.A., Bizzarro, M., 2011. Evidence for magnesium isotope heterogeneity in the solar protoplanetary disk. Astrophys. J. Lett. 735 (2), L37.
Lauretta, D.S., Balram-Knutson, S.S., Beshore, E., Boynton, W.V., Drouet d'Aubigny, C., DellaGiustina, D.N., Sandford, S.A., 2017. OSIRIS-REx: sample return from asteroid (101955) Bennu. Space Sci. Rev. 212, 925–984.
Li, S., Yin, Q.Z., Bao, H., Sanborn, M.E., Irving, A., Ziegler, K., Wang, S., 2018. Evidence for a multilayered internal structure of the chondritic acapulcoite-lodranite parent asteroid. Geochim. Cosmochim. Acta 242, 82–101.
Lichtenberg, T., Drażkowska, J., Schönbächler, M., Golabek, G.J., Hands, T.O., 2021. Bifurcation of planetary building blocks during solar system formation. Science 371 (6527), 365–370.
Lodders, K., 2020. Solar elemental abundances. In: Oxford Research Encyclopedia of Planetary Science.
MacPherson, G.J., 2014. Meteorites and cosmochemical processes. In: Treatise on Geochemistry, 1, pp. 139–179.
Mane, et al., 2016. Zirconium and chromium isotopic systematics of non-Allende CAIs. In: Lunar Planet. Sci. XLVII. Lunar Planet. Inst, Houston, p. 2778 (abstract).
Marrocchi, Y., Euverte, R., Villeneuve, J., Batanova, V., Welsch, B., Ferrière, L., Jacquet, E., 2019. Formation of CV chondrules by recycling of amoeboid olivine aggregate-like precursors. Geochim. Cosmochim. Acta 247, 121–141.
McKeegan, K.D., Kallio, A.P.A., Heber, V.S., Jarzebinski, G., Mao, P.H., Coath, C.D., Burnett, D.S., 2011. The oxygen isotopic composition of the Sun inferred from captured solar wind. Science 332 (6037), 1528–1532.
Mercer, et al., 2010. Chromium and titanium isotope systematics of Allende CAIs. In: Lunar Planet. Sci. XLVI. Lunar Planet. Inst, Houston, p. 2920 (abstract).
Metzler, K., Hezel, D.C., Barosch, J., Wölfer, E., Schneider, J.M., Hellmann, J.L., Kleine, T., 2021. The Loongana (CL) group of carbonaceous chondrites. Geochim. Cosmochim. Acta 304, 1–31.
Morbidelli, A., Baillie, K., Batygin, K., Charnoz, S., Guillot, T., Rubie, D.C., Kleine, T., 2022. Contemporary formation of early Solar System planetesimals at two distinct radial locations. Nat. Astron. 6 (1), 72–79.
Morin, G.L., Marrocchi, Y., Villeneuve, J., Jacquet, E., 2022. 16O-rich anhydrous silicates in CI chondrites: implications for the nature and dynamics of dust in the solar accretion disk. Geochim. Cosmochim. Acta 332, 203–219.
Mougel, B., Moynier, F., Göpel, C., 2018. Chromium isotopic homogeneity between the Moon, the Earth, and enstatite chondrites. Earth Planet. Sci. Lett. 481, 1–8.
Nanne, J.A., Nimmo, F., Cuzzi, J.N., Kleine, T., 2019. Origin of the non-carbonaceous–carbonaceous meteorite dichotomy. Earth Planet. Sci. Lett. 511, 44–54.
Neumann, W., Henke, S., Breuer, D., Gail, H.P., Schwarz, W.H., Trieloff, M., Spohn, T., 2018. Modeling the evolution of the parent body of acapulcoites and lodranites: a case study for partially differentiated asteroids. Icarus 311, 146–169.
Nie, N.X., Chen, X.Y., Hopp, T., Hu, J.Y., Zhang, Z.J., Teng, F.Z., Dauphas, N., 2021. Imprint of chondrule formation on the K and Rb isotopic compositions of carbonaceous meteorites. Sci. Adv. 7 (49), eabl3929.
Papanastassiou, D.A., 1986. Chromium isotopic anomalies in the Allende meteorite. Astrophys. J. Part 2-Letters to the Editor (ISSN 0004-637X), vol. 308, Sept. 1, 1986, p. L27-L30.
Paquet, M., Moynier, F., Yokoyama, T., Dai, W., Hu, Y., Abe, Y., Yurimoto, H., 2022. Contribution of Ryugu-like material to Earth's volatile inventory by Cu and Zn isotopic analysis. Nat. Astron. 1–8.
Petitat, M., Birck, J.L., Luu, T.H., Gounelle, M., 2011. The chromium isotopic composition of the ungrouped carbonaceous chondrite Tagish Lake. Astrophys. J. 736 (1), 23.
Poole, G.M., Rehkämper, M., Coles, B.J., Goldberg, T., Smith, C.L., 2017. Nucleosynthetic molybdenum isotope anomalies in iron meteorites–new evidence for thermal processing of solar nebula material. Earth Planet. Sci. Lett. 473, 215–226.

Qin, L., Alexander, C.M.D., Carlson, R.W., Horan, M.F., Yokoyama, T., 2010. Contributors to chromium isotope variation of meteorites. Geochim. Cosmochim. Acta 74 (3), 1122–1145.
Rubin, A.E., 2007. Petrogenesis of acapulcoites and lodranites: A shock-melting model. Geochim. Cosmochim. Acta 71 (9), 2383–2401.
Rubin, A.E., 2011. Origin of the differences in refractory-lithophile-element abundances among chondrite groups. Icarus 213 (2), 547–558.
Sanborn, M.E., Yin, Q.Z., 2015. Investigating a common source for Brachinites and Graves Nunataks 06128 and 06129 meteorites using high precision chromium isotopes. In: Lunar Planet. Sci. XLVI. Lunar Planet. Inst, Houston, p. 2241 (abstract).
Sanborn, M.E., Yin, Q.Z., 2019. Magmatism in the Outer Solar System: what we know now from isotope forensics of carbonaceous achondrites. In: Lunar Planet. Sci. L. Lunar Planet. Inst, Houston, p. 1498 (abstract).
Sanborn, M.E., Wimpenny, J., Williams, C.D., Yamakawa, A., Amelin, Y., Irving, A.J., Yin, Q.Z., 2019. Carbonaceous achondrites Northwest Africa 6704/6693: milestones for early Solar System chronology and genealogy. Geochim. Cosmochim. Acta 245, 577–596.
Savage, P.S., Moynier, F., Boyet, M., 2022. Zinc isotope anomalies in primitive meteorites identify the outer solar system as an important source of Earth's volatile inventory. Icarus 386, 115172.
Schiller, M., Van Kooten, E., Holst, J.C., Olsen, M.B., Bizzarro, M., 2014. Precise measurement of chromium isotopes by MC-ICPMS. J. Anal. At. Spectrom. 29 (8), 1406–1416.
Schiller, M., Paton, C., Bizzarro, M., 2015. Evidence for nucleosynthetic enrichment of the protosolar molecular cloud core by multiple supernova events. Geochim. Cosmochim. Acta 149, 88–102.
Schiller, M., Bizzarro, M., Fernandes, V.A., 2018. Isotopic evolution of the protoplanetary disk and the building blocks of Earth and the Moon. Nature 555 (7697), 507–510.
Schiller, M., Bizzarro, M., Siebert, J., 2020. Iron isotope evidence for very rapid accretion and differentiation of the proto-Earth. Sci. Adv. 6 (7), eaay7604.
Schneider, J.M., Burkhardt, C., Marrocchi, Y., Brennecka, G.A., Kleine, T., 2020. Early evolution of the solar accretion disk inferred from Cr-Ti-O isotopes in individual chondrules. Earth Planet. Sci. Lett. 551, 116585.
Sears, D.W., 1998. The case for rarity of chondrules and calcium-aluminum-rich inclusions in the early solar system and some implications for astrophysical models. Astrophys. J. 498 (2), 773.
Shollenberger, Q.R., Wittke, A., Render, J., Mane, P., Schuth, S., Weyer, S., Brennecka, G. A., 2019. Combined mass-dependent and nucleosynthetic isotope variations in refractory inclusions and their mineral separates to determine their original Fe isotope compositions. Geochim. Cosmochim. Acta 263, 215–234.
Shuai, K., Hui, H., Zhou, L., Li, W., 2022. Accretion regions of meteorite parent bodies inferred from a two-endmember isotopic mixing model. Mon. Not. R. Astron. Soc. 513 (1), 363–373.
Shukolyukov, A., Lugmair, G.W., 2006. Manganese–chromium isotope systematics of carbonaceous chondrites. Earth Planet. Sci. Lett. 250 (1–2), 200–213.
Shukolyukov, A., et al., 2009. Mn-Cr isotope systematics of angrite Northwest Africa 4801. In: Lunar Planet. Sci. XL. Lunar Planet. Inst, Houston, p. 1381 (abstract).
Steller, T., Burkhardt, C., Yang, C., Kleine, T., 2022. Nucleosynthetic zinc isotope anomalies reveal a dual origin of terrestrial volatiles. Icarus 386, 115171.
Tissot, F.L., Dauphas, N., Grossman, L., 2016. Origin of uranium isotope variations in early solar nebula condensates. Sci. Adv. 2 (3), e1501400.
Torrano, et al., 2018. Combined investigation of chromium, titanium, and magnesium isotope compositions of refractory inclusions from a variety of carbonaceous chondrites. In: Lunar Planet. Sci. XLIX. Lunar Planet. Inst, Houston, p. 2405 (abstract).
Torrano, Z.A., Brennecka, G.A., Williams, C.D., Romaniello, S.J., Rai, V.K., Hines, R.R., Wadhwa, M., 2019. Titanium isotope signatures of calcium-aluminum-rich inclusions from CV and CK chondrites: implications for early Solar System reservoirs and mixing. Geochim. Cosmochim. Acta 263, 13–30.
Torrano, Z.A., Schrader, D.L., Davidson, J., Greenwood, R.C., Dunlap, D.R., Wadhwa, M., 2021. The relationship between CM and CO chondrites: insights from combined analyses of titanium, chromium, and oxygen isotopes in CM, CO, and ungrouped chondrites. Geochim. Cosmochim. Acta 301, 70–90.
Trinquier, A., Birck, J.L., Allegre, C.J., 2007. Widespread 54Cr heterogeneity in the inner solar system. Astrophys. J. 655 (2), 1179.
Trinquier, A., Elliott, T., Ulfbeck, D., Coath, C., Krot, A.N., Bizzarro, M., 2009. Origin of nucleosynthetic isotope heterogeneity in the solar protoplanetary disk. Science 324 (5925), 374–376.
Valdes, M.C., Bermingham, K.R., Huang, S., Simon, J.I., 2021. Calcium isotope cosmochemistry. Chem. Geol. 581, 120396.
Van Kooten, E.M., Wielandt, D., Schiller, M., Nagashima, K., Thomen, A., Larsen, K.K., Bizzarro, M., 2016. Isotopic evidence for primordial molecular cloud material in metal-rich carbonaceous chondrites. Proc. Natl. Acad. Sci. 113 (8), 2011–2016.
Van Kooten, E., Cavalcante, L., Wielandt, D., Bizzarro, M., 2020. The role of bells in the continuous accretion between the CM and CR chondrite reservoirs. Meteorit. Planet. Sci. 55 (3), 575–590.
Warren, P.H., 2011. Stable-isotopic anomalies and the accretionary assemblage of the Earth and Mars: a subordinate role for carbonaceous chondrites. Earth Planet. Sci. Lett. 311 (1–2), 93–100.
Watanabe, S.I., Tsuda, Y., Yoshikawa, M., Tanaka, S., Saiki, T., Nakazawa, S., 2017. Hayabusa2 mission overview. Space Sci. Rev. 208, 3–16.
Williams, C.D., Janney, P.E., Hines, R.R., Wadhwa, M., 2016. Precise titanium isotope compositions of refractory inclusions in the Allende CV3 chondrite by LA-MC-ICPMS. Chem. Geol. 436, 1–10.
Williams, C.D., Sanborn, M.E., Defouilloy, C., Yin, Q.Z., Kita, N.T., Ebel, D.S., Yamashita, K., 2020. Chondrules reveal large-scale outward transport of inner Solar System materials in the protoplanetary disk. Proc. Natl. Acad. Sci. 117 (38), 23426–23435.
Wood, J.A., 2004. Formation of chondritic refractory inclusions: the astrophysical setting. Geochim. Cosmochim. Acta 68 (19), 4007–4021.
Wood, B.J., Smythe, D.J., Harrison, T., 2019. The condensation temperatures of the elements: a reappraisal. Am. Mineral. J. Earth Planet. Mater. 104 (6), 844–856.
Yada, T., Abe, M., Okada, T., Nakato, A., Yogata, K., Miyazaki, A., Tsuda, Y., 2022. Preliminary analysis of the Hayabusa2 samples returned from C-type asteroid Ryugu. Nat. Astron. 6 (2), 214–220.
Yamakawa, A., Yamashita, K., Makishima, A., Nakamura, E., 2010. Chromium isotope systematics of achondrites: chronology and isotopic heterogeneity of the inner solar system bodies. Astrophys. J. 720 (1), 150.
Yamashita, K., Ueda, T., Nakamura, N., Kita, N., Heaman, L.M., 2005. Chromium isotopic study of mesosiderite and ureilite: evidence for 54Cr deficit in differentiated meteorites. In: NIPR Symp. Antarct. Meteorit, 29, pp. 100–101.
Yamashita, K., Maruyama, S., Yamakawa, A., Nakamura, E., 2010. 53Mn–53Cr chronometry of CB chondrite: evidence for uniform distribution of 53Mn in the early solar system. Astrophys. J. 723 (1), 20.
Yang, L., Ciesla, F.J., 2012. The effects of disk building on the distributions of refractory materials in the solar nebula. Meteorit. Planet. Sci. 47 (1), 99–119.
Yokoyama, T., Nagashima, K., Nakai, I., Young, E.D., Abe, Y., Al'eon, J., Yurimoto, H., 2022. Samples returned from the asteroid Ryugu are similar to Ivuna-type carbonaceous meteorites. Science eabn7850.
Zhang, J., Dauphas, N., Davis, A.M., Pourmand, A., 2011. A new method for MC-ICPMS measurement of titanium isotopic composition: identification of correlated isotope anomalies in meteorites. J. Anal. At. Spectrom. 26 (11), 2197–2205.
Zhang, J., Dauphas, N., Davis, A.M., Leya, I., Fedkin, A., 2012. The proto-Earth as a significant source of lunar material. Nat. Geosci. 5 (4), 251–255.
Zhu, K., Liu, J., Moynier, F., Qin, L., Alexander, C.M.D., He, Y., 2019. Chromium isotopic evidence for an early formation of chondrules from the Ornans CO chondrite. Astrophys. J. 873 (1), 82.
Zhu, K., Moynier, F., Schiller, M., Wielandt, D., Larsen, K.K., van Kooten, E.M., Bizzarro, M., 2020. Chromium isotopic constraints on the origin of the ureilite parent body. Astrophys. J. 888 (2), 126.
Zhu, K., Moynier, F., Schiller, M., Alexander, C.M.D., Davidson, J., Schrader, D.L., Bizzarro, M., 2021. Chromium isotopic insights into the origin of chondrite parent bodies and the early terrestrial volatile depletion. Geochim. Cosmochim. Acta 301, 158–186.
Zolensky, M.E., Zega, T.J., Yano, H., Wirick, S., Westphal, A.J., Weisberg, M.K., Bastien, R., 2006. Mineralogy and petrology of comet 81P/Wild 2 nucleus samples. Science 314 (5806), 1735–1739.